

K^\pm Production in Semi-Inclusive Deep Inelastic Scattering using Transversely Polarized Targets and the SoLID Spectrometer

(A Run-Group Proposal Submitted to PAC 46)

June 4, 2018

John Arrington, Whitney Armstrong, Paul Reimer, Seamus Riordan, Junqi Xie, Zhihong Ye^{*†}
Argonne National Laboratory, Physics Division, Argonne, IL, USA

Andrew Puckett
University of Connecticut, Storrs, Connecticut, USA

Haiyan Gao, Chao Gu, Xiaqing Li, Weizhi Xiong, Zhiwen Zhao^{*}
Duke University, Durham, NC, USA

Fatiha Benmokhtar
Duquesne University, Pittsburgh, PA USA

Alexandre Camsonne, Jian-Ping Chen, Tianbo Liu^{*}
Jefferson Lab, Newport News, VA, USA

Miha Mihovilovič, Simon Širca
Faculty of Mathematics and Physics, University of Ljubljana, Slovenia

Mitra Shabestari
Mississippi State University, Starkville, MS, USA

Mohammad Hattawy
Old Dominion University, Norfolk, VA, USA

Garth Huber
University of Regina, Regina, SK, Canada

Abhay Deshpande, Klaus Dehmelt, Nils Feege, Thomas Hemmick, Krishna Kumar,
Sanghwa Park^{*}, Jinlong Zhang
Stony Brook University, Stony Brook, NY, USA

Chendi Shen, Fuyue Wang, Yi Wang^{*}
Tsinghua University, Beijing, China

1

^{1*}: Cospokespeople, †: Contact (yez@jlab.org, yez@anl.gov)

Abstract

We propose to perform the measurement of the K^\pm production in the Semi-Inclusive Deep Inelastic Scattering (SIDIS) using both the transversely polarized proton (NH_3) target and the transversely polarized ^3He target (as effective polarized neutron target) on the SoLID spectrometer. This measurement will be carried out in parallel with the already approved SoLID experiments which will measure the π^\pm production in SIDIS, including E12-10-006 with a transversely polarized ^3He target and E12-11-108 with a transversely polarized NH_3 target. We will perform the off-line analysis to extract the K^\pm Collins asymmetries, Sivers asymmetries and other TMD asymmetries. Model estimation shows that at the SoLID kinematic about 20% of the kaon SIDIS events come from the current fragmentation region where the TMD factorization can be applied. New data from this measurement will provide not only important input to determine the TMD of u and d valence-quarks by combining with the pion measurements from SoLID and elsewhere, but also has the unique sensitivity to sea-quarks, e.g. s and \bar{s} . Our measurement will have a strong contribution to the development of the TMD physics and provide important guidance for studying sea-quarks and gluon TMDs on the future EIC.

This run group proposal does not need additional beam-time nor requires modification to the existing experiment design. The heavy-gas Čerenkov detector and the MRPC in the standard SIDIS setup already have the capability of identifying kaons from pions and protons at certain momentum ranges. We hope to improve the MRPC's time resolution down to 20 ps which should provide precise time-of-flight information for better π^\pm/K^\pm separation up to a high hadron momentum (e.g. $P_h < 7.0 \text{ GeV}/c$). In this proposal, we will demonstrate that such a requirement is achievable in today's detector technologies.

Contents

1	Physics motivation	4
1.1	Transverse Momentum Dependent Parton Distributions (TMD)	4
1.2	TMDs in Kaon SIDIS Production	6
1.3	Spin asymmetries in SIDIS	9
1.4	SIDIS kinematic regions	11
2	Experimental Setup	14
3	Kaon Identification	16
3.1	Overview	16
3.2	Pion rejection by HGC Detector	17
3.3	Time-Of-Flight PID	18
3.4	MRPC Detector	19
3.5	Recent MRPC R&D Progresses	19
3.6	MRPC Simulation Framework	21
3.7	Kaon Identification with TOF and HGC	24
4	Projected Results	25
4.1	Kinematic Coverage	25
4.2	Rate Estimations	31
4.3	Projected Asymmetries	32
4.4	Systematic Uncertainties	38
5	Summary	38

1 Physics motivation

Quantum chromodynamics (QCD) is nowadays viewed as the fundamental theory of strong interaction in the framework of Yang-Mills gauge theory. Unveiling the nucleon structure in terms of quarks and gluons is one of the main goals of nuclear and particle physics. Due to the nonperturbative nature of QCD at low energy scale, *e.g.* the hadron scale, a first principle calculation of nucleon structures is still a challenging issue. Several theoretical methods, such as the Euclidean lattice gauge theory [1], the Dyson-Schwinger equation [2], and the gauge/gravity duality [3], are developed to study the nonperturbative properties of QCD. Experimental tests will be essential to help us understand the nonperturbative dynamics of the strong interaction.

1.1 Transverse Momentum Dependent Parton Distributions (TMD)

Parton distribution functions (PDFs), which at the leading twist are interpreted as the probability density of finding a parton (quark or gluon) carrying the momentum fraction x at a resolution scale Q , are proven powerful tools in describing the inclusive deep inelastic scattering (DIS) process, the Drell-Yan process, and other high energy scattering processes. With the (collinear) factorization theorem, the cross sections of these high energy hadronic scattering processes can be expressed up to some power suppressed correction terms as a convolution of a process dependent but perturbative calculable partonic hard scattering part and process independent functions, *e.g.* PDFs, which encode the structure of a hadron. As a generalization of collinear PDFs, transverse momentum dependent parton distributions (TMDs) and generalized parton distributions (GPDs) are introduced to have three-dimensional descriptions of partonic structures of the nucleon. TMDs, which at the leading twist could be interpreted as a three-dimensional momentum distributions of the parton, are utilized in the study of low transverse momentum semi-inclusive DIS (SIDIS) process and Drell-Yan process within the TMD factorization theorem. GPDs, which incorporate the transverse position information of the parton, are applied in the description of some exclusive hadronic scattering processes, such as the deeply virtual Compton scattering (DVCS) process and the deeply virtual meson production (DVMP) process. More complete one parton distribution information in the nucleon is described by Wigner distributions, or with a Fourier transform by generalized transverse momentum dependent parton distributions (GTMDs), and some theoretical explorations have been performed.

The spin structure of the nucleon has received great interests from both theoretical and experimental aspects since the discovery that the quark spin only contributes a small fraction [4, 5], about 30% in recent analyses [6, 7], to the nucleon spin. The remaining nucleon spin could be attributed to the orbital angular momenta and the gluon spin. Experimentally, many efforts have been made to measure the quark helicity term, and the gluon helicity term has also started being known in recent years [8]. In order to have a full understanding of the nucleon spin structure, one must have access to the orbital terms which are almost unknown up to now. Hence, three-dimensional images, via TMDs or GPDs, of the partonic structure in a nucleon are required. SIDIS is one of the main processes to extract TMDs.

Within the TMD factorization, SIDIS structure functions are expressed as convolutions of transverse momentum dependent parton distribution functions (TMD PDFs) and transverse momentum dependent fragmentation functions (TMD FFs). As illustrated in Figure 1, there are eight leading-twist (twist-two) quark TMD PDFs for a nucleon. If the transverse momentum is integrated, three of them (the black


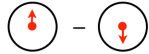
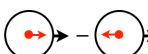

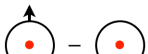
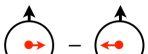
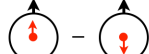
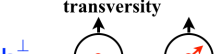
		Quark Polarization		
		U	L	T
Nucleon Polarization	U	f_1  unpolarized		h_1^\perp  Boer-Mulders
	L		g_{1L}  helicity	h_{1L}^\perp  longi-transversity (worm-gear)
	T	f_{1T}^\perp  Sivers	g_{1T}  trans-helicity (worm-gear)	h_1  transversity h_{1T}^\perp  pretzelosity

Figure 1: Leading twist quark TMDs in a nucleon. U, L, and T denote respectively the unpolarized, longitudinal polarized, and transversely polarized configurations.

ones in Figure 1), f_1 , g_{1L} , and h_1 , will reduce to their collinear limits: the unpolarized PDF, helicity distribution, and transversity distribution, while the remaining five will vanish. Hence TMDs, especially the spin-dependent ones, contain much richer information than collinear PDFs, and allow us to access the correlation between quark transverse momentum and quark/nucleon spin. The Sivers function f_{1T}^\perp and the Boer-Mulders function h_1^\perp (the red ones in Figure 1) are naively time-reversal odd TMDs, which were believed vanishing for a long time because of the time-reversal invariance property of QCD [9]. However, a model calculation indicates that nonvanishing Sivers function and Boer-Mulders function can arise from the final or initial state interactions between the struck quark and the target remnant in SIDIS or Drell-Yan process at the leading twist level [10, 11]. It was later proved that a path-order Wilson line is required in the definition of TMDs to ensure the gauge invariance [12], and it provides nontrivial phases which lead to the so-called time-reversal odd TMDs. It is a QCD version of the Aharonov-Bohm effect. In SIDIS, the Sivers function by convoluting with the unpolarized fragmentation function has leading twist contribution to a target transverse single spin asymmetry, which is referred to as the Sivers asymmetry [13]. The measurement of this asymmetry is one of the main approaches to access the Sivers function. Due to the presence of the Wilson line, opposite signs are predicted for the Sivers function as well as the Boer-Mulders function in SIDIS and Drell-Yan processes [12]. Therefore a precise measurement of the Sivers function (and the Boer-Mulders function) in both SIDIS and Drell-Yan processes is a powerful test of the QCD factorization theorem.

The transversity distribution h_1 has both collinear and TMD definitions. As a probability interpretation, it represents the transversely polarized quark density in a transversely polarized nucleon. It can be viewed as the transverse counterpart to the helicity distribution that describes the longitudinally polarized quark density in a longitudinally polarized nucleon, but they are different in relativistic dynamics. The quark transversity distribution is a chiral odd quantity which does not mix with gluons but decouples from the inclusive DIS at the leading twist. In SIDIS, the transversity distribution can be measured from a target transverse single spin asymmetry, referred to as the Collins asymmetry [9], which arises from the convolution between the transversity distribution and the Collins fragmentation function.

The tensor charge, which is defined via the matrix element of a tensor current, equals to the integral of

the transversity distribution in the parton model. It is a fundamental QCD quantity of the nucleon, and a precise measurement of the tensor charge is not only important for understanding the strong interaction but also for the search of new physics beyond the standard model [14].

The pretzelosity distribution is another chiral odd twist-two TMD. In the wave function representation, it is the overlap of wave functions that differ by two units of orbital angular momentum (OAM), $|\Delta L| = 2$ [15], and thus provides an access to quark OAM which plays a significant role in understanding the nucleon spin structure. If neglecting the $|L| > 1$ components of the nucleon, the pretzelosity distribution can only originate from the overlap between $L = 1$ and $L = -1$ wave functions, and a more explicit relation between the pretzelosity and quark OAM can be derived as has been given in some models [16–18]. In SIDIS, the pretzelosity distribution can be measured from a target transverse single spin asymmetry, referred to as the pretzelosity asymmetry, which arises from the convolution between the pretzelosity distribution and the Collins fragmentation function at the leading twist.

1.2 TMDs in Kaon SIDIS Production

The Sivers asymmetry, Collins asymmetry, and pretzelosity asymmetry are also core measurements in the approved pion SIDIS experiments [19, 20] on SoLID, as well as in other experiments [21, 22]. However, only pion SIDIS measurements with both proton and neutron (^3He) targets are not enough for us to have all light flavor separations. Assuming TMD factorization, the total SIDIS cross section is a charge weighted sum of the contributions from all flavors. Since the distribution function of the valence flavor is greater than that of the sea and the favored fragmentation function is greater than the unfavored fragmentation function, one will expect the main contribution is from the convolution between a valence flavor distribution function and a favored fragmentation function.

As K^+ contains a valence \bar{s} quark and K^- contains a valence s quark, in kaon SIDIS productions the strange/antistrange quark is convoluted with a favored fragmentation function, and especially for K^- the two favored fragmentations (s and \bar{u}) are both convoluted to sea-quark distributions in the nucleon. Together with the approved pion SIDIS experiments [19, 20] on proton and ^3He (neutron) targets, the measurements of charged kaon SIDIS productions from the proton and ^3He (neutron) targets will allow us to separate contributions from all light flavors: u , d , s , \bar{u} , \bar{d} , and \bar{s} .

Explorations on kaon SIDIS from transversely polarized targets have been performed by HERMES [23], COMPASS [24], and JLab Hall A collaborations [26]. As a natural expectation, one may expect the sea-quark polarization is much smaller than the valence quark polarization, which is indeed the case in the extraction of collinear helicity distributions. However, as shown in Figures 2, 3, and 4, the single spin asymmetries of the kaon SIDIS measured by HERMES, COMPASS, and JLab Hall A are comparable (or even larger) in size with the asymmetries of the pion SIDIS, which contradicts with our naive expectations. Therefore, a more precise measurement will help to clarify this issue and further improve our understanding of the nucleon spin structure, especially the contributions from each flavor.

The kaon SIDIS is also proposed to be measured in some planned JLab-12 experiments with SBS using a transverse polarized ^3He target [21] and with CLAS12 using a transversely polarized HD-Ice target [22]. However, similar to the pion SIDIS case, kaon SIDIS with SoLID will have higher statistics and a complementary kinematic coverage as well as some overlap region. Furthermore, measuring the pion and kaon SIDIS from both proton and neutron (^3He) targets with the same Detector setup covering the same kinematic

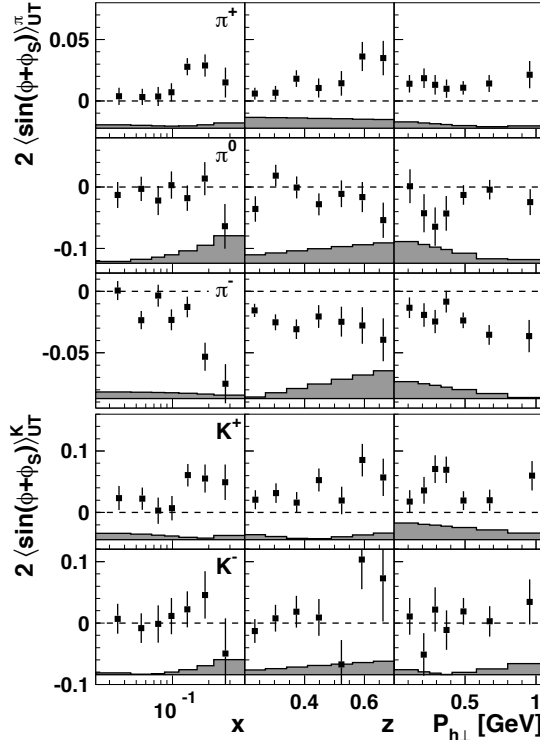


Figure 2: Collins asymmetry of pion and kaon SIDIS measured by HERMES using a transversely polarized proton target. The figure is from Ref. [23].

region is very important to have a direct comparison between the pion and kaon SIDIS data, perform flavor separation of multiple quark TMDs and isolate the sea-quark contributions from the valance quarks'. Together with other 12 GeV kaon SIDIS experiments, our new measurement will provide high quality data for the continuous theoretical development of the TMD physics, and more importantly, provide strong guidance to future measurements on electron-ion collider (EIC), which will fully study the TMD of sea-quarks and gluons in a wider kinematic coverage and provide a more complete image of nucleon structures.

In addition to strong interaction dynamics, an extraction of the strange quark tensor charge through the Collins asymmetry measurement in kaon SIDIS as mentioned above is useful in new physics explorations. For example, a permanent electric dipole moment (EDM) of any particle with a nondegenerate ground state violates both parity and time-reversal symmetries. Assuming CPT invariance, a consequence of local quantum field theories with Lorentz invariance, it is a signal of CP violation. As the Cabibbo-Kobayashi-Maskawa (CKM) complex phase requires the participation of three fermion generations, the EDM of light quarks is highly suppressed by the flavor changing interactions at the three-loop level, and thus the KM mechanism only results in an extremely small EDM. Hence, the quark EDM is one of the most sensitive probes to new physics beyond the SM. Since quarks are confined in hadron, one has to access quark EDMs via nucleon EDM measurements, and the tensor charge serves as the weighting factor,

$$d_N = \sum_q g_T^q d_q, \quad (1)$$

where g_T^q is the tensor charge of flavor- q , d_q is the EDM of flavor- q , and d_N is the nucleon EDM. Up to now,

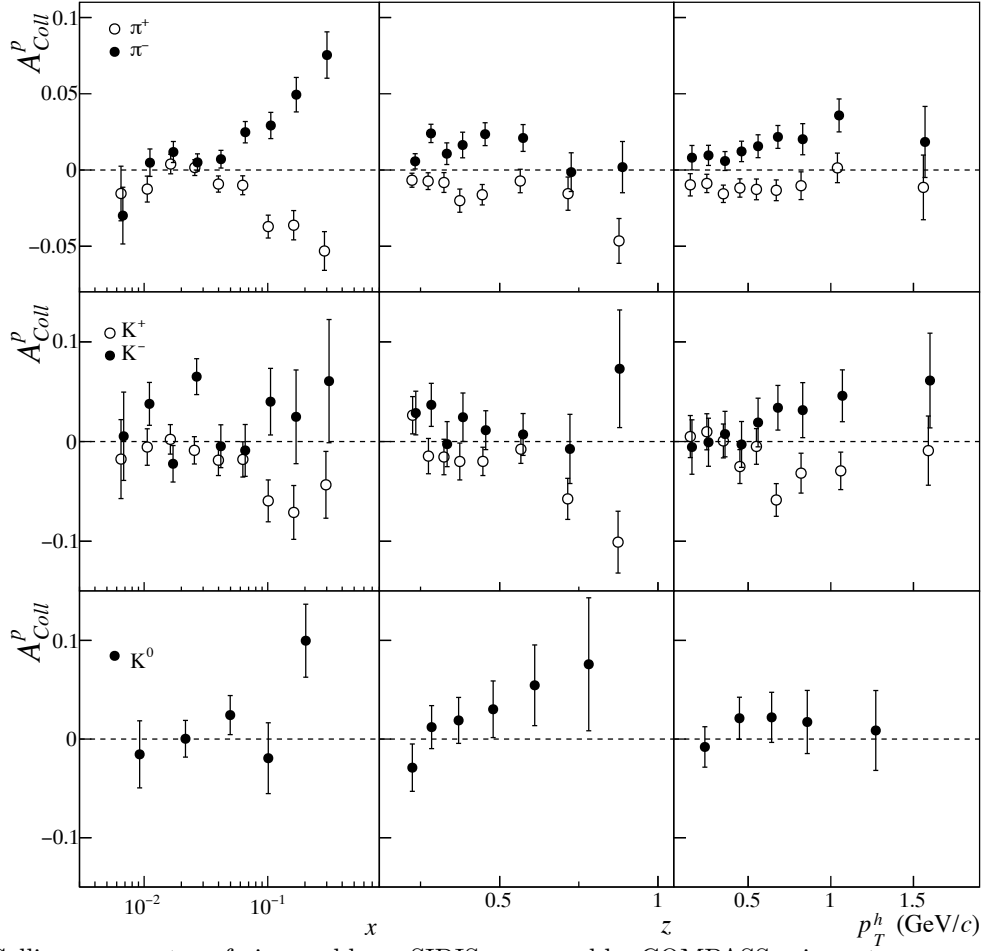


Figure 3: Collins asymmetry of pion and kaon SIDIS measured by COMPASS using a transversely polarized proton target. The figure is from Ref. [24].

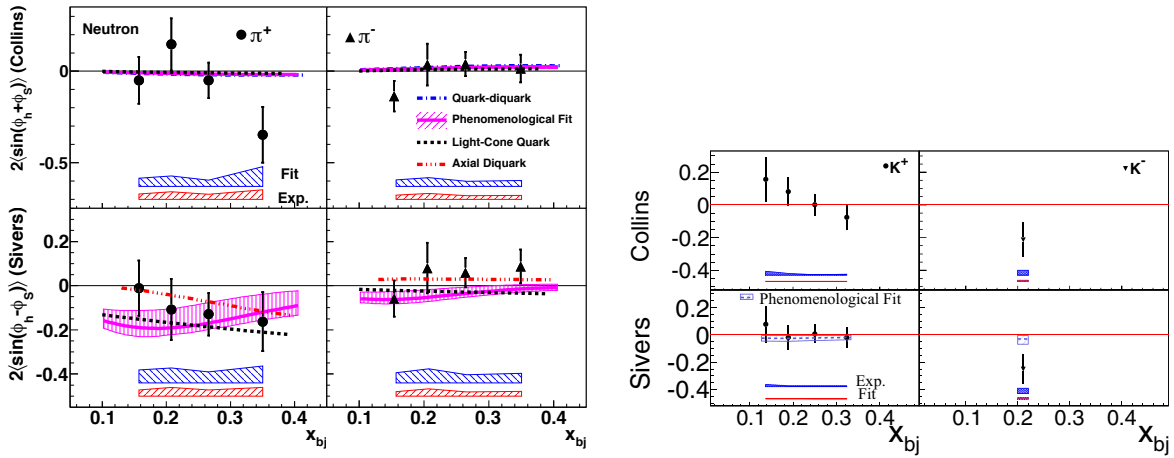


Figure 4: Collins and Sivers asymmetries of pion and kaon SIDIS measured by JLab Hall A using a transversely polarized ^3He target. The figures are from Refs. [25, 26].

all global analysis of transversity distributions and thus tensor charge extractions assume zero strangeness contribution due to the limited precision of the data. On the other hand, the strange quark EDM is expected to be much larger than that of the down quark in most new physics models, because the quark EDM is roughly proportional to the quark mass based on a simple dimensional analysis following the effective field theory. Therefore the extraction of the strange quark tensor charge is important in quantifying the strange quark EDM contribution to the nucleon EDM and then testing new physics models.

1.3 Spin asymmetries in SIDIS

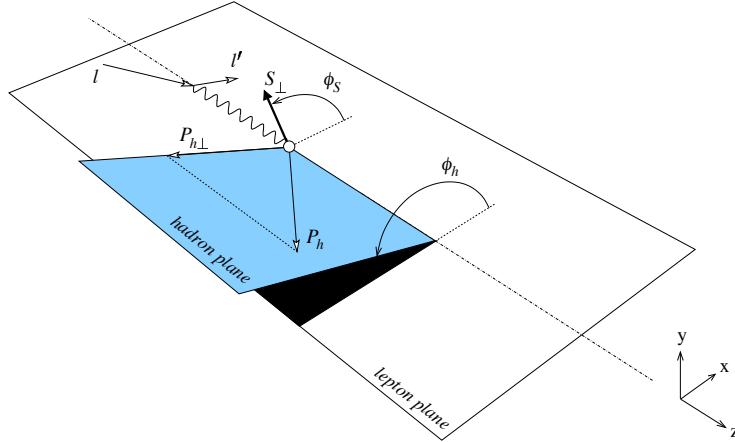


Figure 5: Definitions of azimuthal angles and the transverse momentum of the detected hadron in SIDIS process. They follow the Trento convention [27]. The figure is taken from Ref. [28].

In the semi-inclusive deep inelastic scattering, the lepton is scattered off the nucleon, and one of the hadrons produced in the collision is detected in coincidence with the scattered lepton. The process is expressed as

$$e(l) + N(P) \rightarrow e(l') + h(P_h) + X(P_X), \quad (2)$$

where the lepton in the reaction is set as electrons (e), N is the nucleon, h is the detected hadron, and X represents undetected particles. Four momenta of them are given in parentheses. As usual, the kinematics are expressed in terms of Lorentz scalar variables,

$$Q^2 = -q^2 = -(l - l')^2, \quad x = \frac{Q^2}{2P \cdot q}, \quad z = \frac{P \cdot P_h}{P \cdot q}, \quad (3)$$

where q is the transferred four-momentum, and with one-photon exchange approximation it is the four-momentum of the virtual photon. As illustrated in Figure 5, azimuthal angles and the transverse momentum of the hadron are defined following the Trento convention [27]. The hadron transverse momentum $\mathbf{P}_{h\perp}$ is defined in the photon-nucleon collinear frame, ϕ_h is the azimuthal angle from the lepton plane to the hadron plane, and ϕ_S is the azimuthal angle from lepton plane to the nucleon polarization direction if it is transversely polarized.

Assuming one-photon exchange, the differential cross section of SIDIS can be expressed in terms of 18

structure functions according to different beam and target polarizations and azimuthal modulations,

$$\begin{aligned}
\frac{d\sigma}{dx dy dz d\psi d\phi_h d\mathbf{P}_{h\perp}^2} &= \frac{\alpha^2}{xyQ^2} \frac{y^2}{2(1-\epsilon)} \left(1 + \frac{\gamma^2}{2x}\right) \left\{ F_{UU,T} + \epsilon F_{UU,L} + \sqrt{2\epsilon(1+\epsilon)} \cos\phi_h F_{UU}^{\cos\phi_h} \right. \\
&\quad + \epsilon \cos 2\phi_h F_{UU}^{\cos 2\phi_h} + \lambda_e \sqrt{2\epsilon(1-\epsilon)} \sin\phi_h F_{LU}^{\sin\phi_h} \\
&\quad + S_L \left[\sqrt{2\epsilon(1+\epsilon)} \sin\phi_h F_{UL}^{\sin\phi_h} + \epsilon \sin 2\phi_h F_{UL}^{\sin 2\phi_h} \right] \\
&\quad + S_L \lambda_e \left[\sqrt{1-\epsilon^2} F_{LL} + \sqrt{2\epsilon(1-\epsilon)} \cos\phi_h F_{LL}^{\cos\phi_h} \right] \\
&\quad + S_T \left[\sin(\phi_h - \phi_S) (F_{UT,T}^{\sin(\phi_h - \phi_S)} + \epsilon F_{UT,L}^{\sin(\phi_h - \phi_S)}) \right. \\
&\quad + \epsilon \sin(\phi_h + \phi_S) F_{UT}^{\sin(\phi_h + \phi_S)} + \epsilon \sin(3\phi_h - \phi_S) F_{UT}^{\sin(3\phi_h - \phi_S)} \\
&\quad \left. + \sqrt{2\epsilon(1+\epsilon)} \sin\phi_S F_{UT}^{\sin\phi_S} \sqrt{2\epsilon(1+\epsilon)} \sin(2\phi_h - \phi_S) F_{UT}^{\sin(2\phi_h - \phi_S)} \right] \\
&\quad + S_T \lambda_e \left[\sqrt{1-\epsilon^2} \cos(\phi_h - \phi_S) F_{LT}^{\cos(\phi_h - \phi_S)} + \sqrt{2\epsilon(1-\epsilon)} \cos\phi_S F_{LT}^{\cos\phi_S} \right. \\
&\quad \left. + \sqrt{2\epsilon(1-\epsilon)} \cos(2\phi_h - \phi_S) F_{LT}^{\cos(2\phi_h - \phi_S)} \right] \left. \right\}, \tag{4}
\end{aligned}$$

where α is the electromagnetic fine structure constant, λ_e denotes the lepton beam helicity, S_L and S_T are target longitudinal and transverse polarizations, and the structure functions F are four dimensional functions of x , Q^2 , z , and $\mathbf{P}_{h\perp}^2$. The angle ψ is the azimuthal angle of the scattered lepton around the lepton beam axis with respect to a fixed direction. The exact relation between ψ and ϕ_S is derived in Ref. [29]. In the deep inelastic kinematics, one has $d\psi \approx d\phi_S$. The subscripts of the structure functions indicate the beam and target polarizations, and the third subscript specifies the virtual photon polarization. The ϵ is the ratio of longitudinal and transverse photon flux,

$$\epsilon = \frac{1 - y - \frac{1}{4}\gamma^2 y^2}{1 - y + \frac{1}{2}y^2 + \frac{1}{4}\gamma^2 y^2}, \tag{5}$$

where $\gamma = 2Mx/Q$ and M is the nucleon mass.

Integration over the azimuthal angles, the cross section is expressed as

$$\frac{d\sigma}{dx dy dz d\mathbf{P}_{h\perp}^2} = \frac{4\pi^2 \alpha^2}{xyQ^2} \frac{y^2}{2(1-\epsilon)} \left(1 + \frac{\gamma^2}{2x}\right) F_{UU}(x, Q^2, z, \mathbf{P}_{h\perp}^2) = 4\pi^2 \sigma_0. \tag{6}$$

For a unpolarized beam scattered off a transversely polarized target, one can define the asymmetries,

$$\begin{aligned}
\frac{d\sigma}{dx dy dz d\mathbf{P}_{h\perp}^2 d\phi_h d\phi_S} &= \sigma_0 \left\{ 1 + \cos\phi_h A_{UU}^{\cos\phi_h} + \cos 2\phi_h A_{UU}^{\cos 2\phi_h} \right. \\
&\quad + S_T \left[\sin(\phi_h - \phi_S) A_{UT}^{\sin(\phi_h - \phi_S)} + \sin(\phi_h + \phi_S) A_{UT}^{\sin(\phi_h + \phi_S)} \right. \\
&\quad \left. + \sin(3\phi_h - \phi_S) A_{UT}^{\sin(3\phi_h - \phi_S)} + \sin\phi_S A_{UT}^{\sin\phi_S} + \sin(2\phi_h - \phi_S) A_{UT}^{\sin(2\phi_h - \phi_S)} \right] \left. \right\}, \tag{7}
\end{aligned}$$

where

$$A_{UU}^{\cos \phi_h} = \frac{\sqrt{2\varepsilon(1+\varepsilon)}F_{UU}^{\cos \phi_h}}{F_{UU}}, \quad (8)$$

$$A_{UU}^{\cos 2\phi_h} = \frac{\varepsilon F_{UU}^{\cos 2\phi_h}}{F_{UU}}, \quad (9)$$

are unpolarized azimuthal modulations, and

$$A_{UT}^{\sin(\phi_h-\phi_s)} = \frac{F_{UT}^{\sin(\phi_h-\phi_s)}}{F_{UU}}, \quad (10)$$

$$A_{UT}^{\sin(\phi_h+\phi_s)} = \frac{\varepsilon F_{UT}^{\sin(\phi_h+\phi_s)}}{F_{UU}}, \quad (11)$$

$$A_{UT}^{\sin(3\phi_h-\phi_s)} = \frac{\varepsilon F_{UT}^{\sin(3\phi_h-\phi_s)}}{F_{UU}}, \quad (12)$$

$$A_{UT}^{\sin \phi_s} = \frac{\sqrt{2\varepsilon(1+\varepsilon)}F_{UT}^{\sin \phi_s}}{F_{UU}}, \quad (13)$$

$$A_{UT}^{\sin(2\phi_h-\phi_s)} = \frac{\sqrt{2\varepsilon(1+\varepsilon)}F_{UT}^{\sin \phi_s}}{F_{UU}}, \quad (14)$$

$$(15)$$

are target transverse single spin asymmetries.

Assuming TMD factorization, one has three target transverse spin asymmetries at the leading twist level: $A_{UT}^{\sin(\phi_h-\phi_s)}$, $A_{UT}^{\sin(\phi_h+\phi_s)}$, and $A_{UT}^{\sin(3\phi_h-\phi_s)}$. They respectively correspond to the Sivers, Collins, and pretzelocity asymmetries, which as discussed above are proportional to the convolutions $f_{1T}^\perp \otimes D_1$, $h_1 \otimes H_1^\perp$, and $h_{1T}^\perp \otimes H_1^\perp$ at the leading twist. Here D_1 is the unpolarized fragmentation function and H_1^\perp is the Collins fragmentation function.

1.4 SIDIS kinematic regions

As discussed above, the TMD factorization is the underlying theorem that allows us to extract TMDs from SIDIS measurements, but the factorization is only valid for certain kinematic regions. For the photon virtuality to be acceptable as a hard scale, $Q^2 \gg \Lambda_{\text{QCD}}^2$ must be satisfied. In this proposal, we require $Q^2 > 1 \text{ GeV}^2$. When the detected hadron transverse momentum $\mathbf{P}_{h\perp}$ is large, it is associated with the transverse momentum generated from hard radiations, and then one can apply the collinear factorization. For the kinematic coverage by SoLID detector, we are measuring the SIDIS process with small $\mathbf{P}_{h\perp}$. As illustrated in Figure 6, one can define three regions: (a) current fragmentation, (b) target fragmentation, and (c) central (or soft) regions [30].

Current fragmentation region: the outgoing struck quark fragments into the detected hadron, which continues moving roughly in the same direction with roughly the same rapidity. It has a fully developed TMD factorization treatment. The structure functions can be expressed in terms of TMD PDFs and TMD FFs. This region has received the most theoretical attention and is also the region we can extract the Sivers function, the transversity distribution, and the pretzelocity distribution discussed above.

Target fragmentation region: the detected hadron is generated from the remnant of the nucleon, and its momentum is roughly collinear to the target. It is described in terms of extended fracture functions.

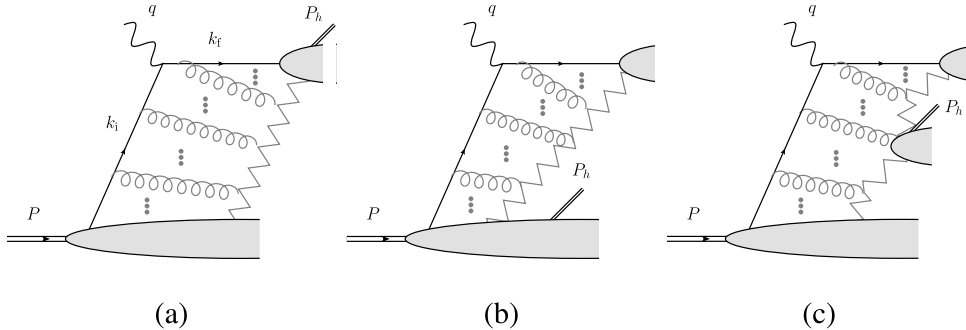


Figure 6: Kinematic regions of SIDIS at small $\mathbf{P}_{h\perp}$. (a) The current fragmentation region; (b) the target fragmentation region; (c) the central (soft) region. The figure is from Ref. [30].

Central (or soft) fragmentation region: the produced hadron’s rapidity is much less than that of the target but much greater than that of the outgoing quark (or current jet). A factorization theorem for the central fragmentation region is in principle possible but has not been worked out yet.

An important point is that the classification of the three regions is not sharp. They overlap with each other, and the real SIDIS process is a mix of them. But at certain kinematics, one can identify one of them dominates the process. Once factorization theorems are developed for all three regions, one can match the factorization from one region to another region to have a unified description.

Although one cannot clearly separate the three regions, a ratio factor

$$R_1 = \frac{P_h \cdot k_f}{P_h \cdot k_i} \quad (16)$$

is defined by theorists as criteria to identify which region is the dominant one for a given SIDIS process [30,31]. Here k_f and k_i are the four-momenta of the outgoing quark and the incoming quark as labeled in Figure 6. When R_1 is small, one can identify the process in the current fragmentation region, because in this case the hadron momentum P_h is roughly parallel to the outgoing quark and thus the numerator $P_h \cdot k_f$ is small. When R_1 is large, *i.e.* $1/R_1$ is small, one can identify the process in the target fragmentation region, because in this case the hadron momentum P_h is roughly parallel to the target as well as the incoming quark and thus the denominator $P_h \cdot k_i$ is small. When $R_1 \sim 1$, one can identify it in the central region.

To estimate the value of R_1 , one has to make some assumptions. Here we follow the procedure in Ref. [31] and perform a Monte Carlo sampling with SoLID kinematics. In Figure 7, we show the R_1 distributions of SoLID kaon SIDIS events. Kinematic cuts: $Q^2 > 1 \text{ GeV}^2$, $W > 2.3 \text{ GeV}$, $W' > 1.6 \text{ GeV}$, and $0.3 < z < 0.7$ have been applied. Using $R_1 < 0.4$ and $1/R_1 < 0.4$ to separate the current fragmentation region and the target fragmentation region from the full range, we will have about 20% events in the current fragmentation region and about 10% events in the target fragmentation region.

The kaon SIDIS events in the current fragmentation region can be used to extracted quark Sivers, transversity, pretzelocity and other TMDs. A wide coverage from the current fragmentation region to the central region and even to the target fragmentation region will help to learn the transition from one region to another region and to estimate the corrections in the TMD extractions using the data in the current fragmentation region. Combining the data that will be collected here at low- Q^2 and future EIC data at high- Q^2 , one will have a wide kinematic range, which is important in quantifying the correction terms.

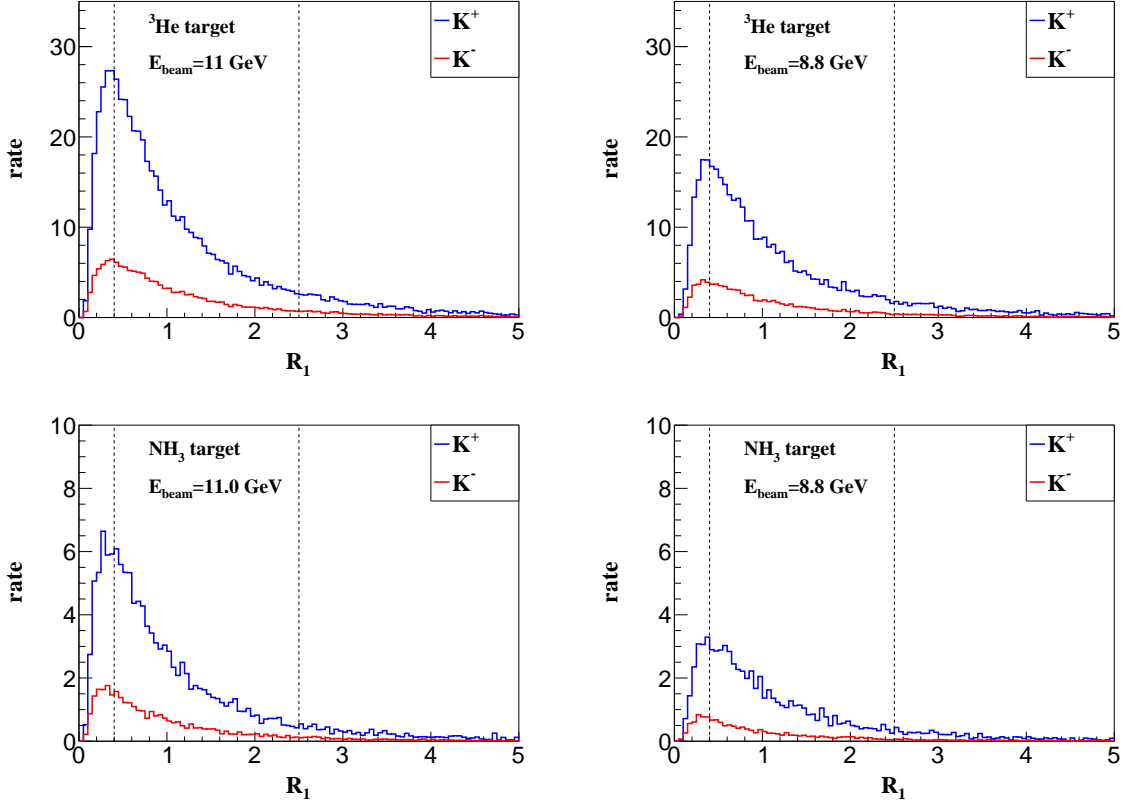


Figure 7: SoLID kaon SIDIS kinematic regions (R_1 distributions). The left panel is with 11 GeV beam, and the right panel is with 8.8 GeV beam. The blue curves are R_1 distributions for K^+ -SIDIS, and the red curves are those for K^- -SIDIS. Kinematics cuts: $Q^2 > 1 \text{ GeV}^2$, $W > 2.3 \text{ GeV}$, $W' > 1.6 \text{ GeV}$, and $0.3 < z < 0.7$, have been applied. The vertical dashed lines correspond to $R_1 = 0.4$ and $R_1^{-1} = 0.4$. From left (small R_1) to right (large R_1), it transits from the current fragmentation region to the central fragmentation region and finally to the target fragmentation region.

2 Experimental Setup

We propose to measure the K^\pm production in the Semi-Inclusive Deep-Inelastic Scattering (SIDIS) with both polarized proton and neutron targets by using Solenoidal Large Intensity Device (SoLID) [32]. It will be a natural extension of the already approved SIDIS experiments on SoLID to measure π^\pm production with polarized neutron target (E12-10-006 [19], E12-11-007 [33]) and with the polarized proton target (E12-11-108 [20]).

SoLID has two configurations of the detector system, called SoLID-SIDIS and SoLID-PVDIS. Besides E12-10-006, two SIDIS experiments, E12-11-007 [33] and E12-11-108 [20], along with the J/ψ experiment (E12-12-006 [34]), will also use the SoLID-SIDIS configuration. All of these experiments have been approved with A or A- rating. In addition, two “bonus-run” experiments, E12-10-006A [35] and E12-11-108A [36], have also been approved to run in parallel with the SIDIS experiments. Another “bonus-run” experiment, E12-10-006B [38] was also approved to perform the measurement of deep virtual meson production (DVMP) to study GPD as with the SoLID-SIDIS setup. The SoLID-PVDIS configuration is for the Parity Violation in Deep Inelastic Scattering (PVDIS) [37].

The solenoid magnet for SoLID is based on the CLEO-II magnet built by Cornell University. The magnet has coil length of 3.5 m with an inner cryostat diameter of 2.9 m. The max field strength is about 1.4 Tesla, with an integrated BDL close to 5 Tesla-meters. The fringe field at the front end after shielding can be controlled less than 5 Gauss. In the SIDIS-configuration, the CLEO-II magnet provides 2π acceptance in the azimuthal angle (ϕ) and covers polar angle (θ) from 8° up to 24° . The momentum acceptance is between 0.8 and 7.5 GeV/c for electrons and hadrons. The momentum resolution is about 2% and angle resolution is about a few mrad.

The layout of the SoLID detectors in the SIDIS-configuration is shown in Fig. 8. The detector system is divided into two regions for the forward-angle (FA) detection and the large-angle (LA) detection. Six tracking chambers based on Gas Electron Multipliers (GEM) will be used for charged particle tracking in the forward-angle region, and the first four of them will be shared by the large-angle region. In each region, a Shashlyk-type sampling EM calorimeter (LAEC or FAEC) will measure the particle energy and identify electrons from hadrons. Two scintillator-pad detectors, LASPD and FASPD, will be installed in front of each EC to reject photons and provide timing information for the large-angle. The forward-angle detectors will detect both the electrons and hadrons. A light-gas Čerenkov detector (LGC) and a heavy-gas Čerenkov detector (HGC) will perform the e/π^\pm and π^\pm/K^\pm separation, respectively. The Multi-gap Resistive Plate Chamber (MRPC) will provide a precise time measurement for the forward going charged particles and it will also provide some photon rejection.

The proposed measurement on neutron will utilize the polarized ^3He target as an effective neutron target. Such a target was successfully employed in E06-110, a 6 GeV SIDIS experiment in Hall A. The polarized ^3He target is based on the technique of spin-exchange optical pumping of hybrid Rb-K alkali atoms. There are two sets of Helmholtz coils with a magnetic field in the order of 25 Gauss to provide the transverse and longitudinal polarization. The ^3He gas with a density of about 10 amg (10 atm at 0°) is stored in a 40 cm target cell made of thin glasses. With a 15 μA electron beam, the neutron luminosity can be as high as $10^{36} \text{ cm}^{-2}\text{s}^{-1}$. The in-beam polarization of 60% was archived during the E06-110 experiment. Two kinds of polarimetry, NMR and EPR, were used to measure the polarization with relative 5% precision. We have plans to improve the accuracy of the measurement to reach 3%. The proposed measurement on proton will

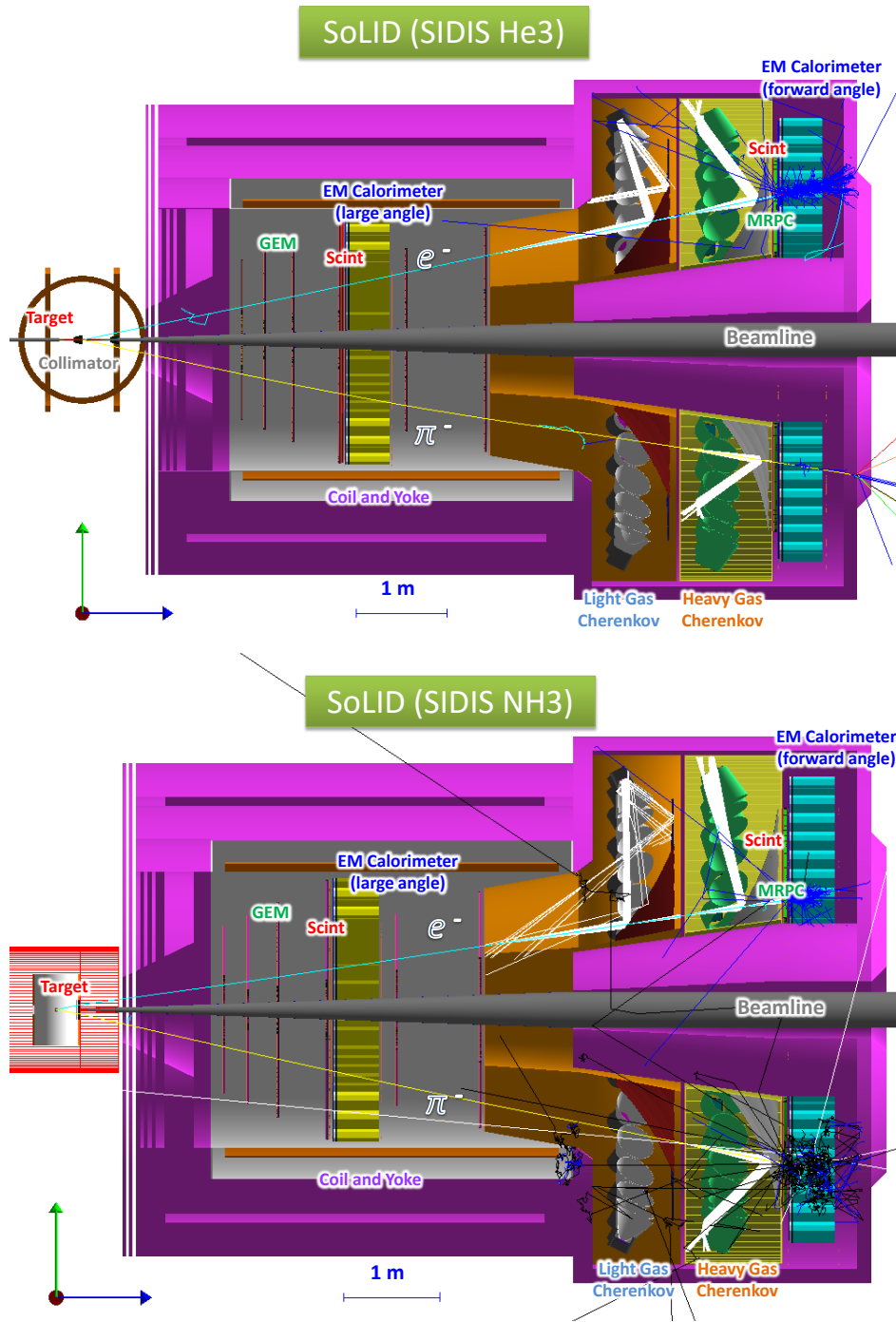


Figure 8: The Detector Layout of the SoLID-SIDIS configuration with either ^3He or NH_3 target. The detector system includes six Gas Electron Multiplier (GEM) planes for charged particle tracking, two Scintillator Pad Detectors (SPD) followed by two Shashlyk sampling EM Calorimeters (EC) for electron and photon energy measurement and particle identification, a Light Gas Čerenkov Detector (LGC) for $e-\pi^\pm$ separation, a Heavy Gas Čerenkov Detector (HGC) for $\pi^\pm-K^\pm$ separation, as well as a Multi-gap Resistive Plate Chamber (MRPC) for time measurement. The 1 - 4 GEM trackers, the large-angle SPD (LASPD) and large-angle EC (LAEC) form the large-angle detection system for electron measurement. The forward-angle detection system, to measure electron and hadrons, is composed of all 2-6 GEM trackers, LGC, HGC, MRPC, the forward-angle SPD (FASPD) and the forward-angle EC (FAEC). The polarized ^3He target is shown with both longitudinal and transverse field coils. The transversely polarized NH_3 target is shown with its solenoid field and scattering chamber.

use the dynamically polarized ammonia target. It has been used at SLAC and at Jefferson on numerous occasions. Its last use as a longitudinally polarized target was in 2012 for the g2p/Gep experiments, which took place in Hall A. Proton luminosities of $10^{35} \text{ cm}^{-2}\text{s}^{-1}$ with 90% polarization have been achieved with this target, in conjunction with electron beam currents up to 100 nA. For the SoLID measurement, a new 5T magnet will be constructed to make it a transversely polarized target.

A more detailed discussion of the design, simulation, prototype-test of each detector and targets is given in the SoLID preliminary conceptual design report (pCDR) [32].

As a run group proposal, this new measurement has no requirement of extra beam-time or configuration change. The existing detector systems like the HGC and the MRPC already can identify kaons from other charged particles at certain momentum limits. However, to cleanly detect large-momentum kaons this experiment does require an improvement on the time resolution of the time-of-flight (TOF) detector. The MRPC will need to improve its time resolution down to 20 ps so that we can use the TOF information to sufficiently separate kaons from pions up to 7 GeV/c. In the next section, we will demonstrate that such a new requirement will be achievable with current technologies.

3 Kaon Identification

3.1 Overview

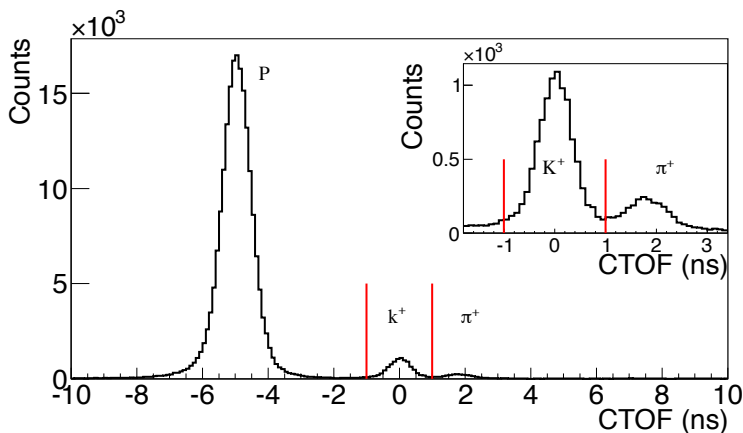


Figure 9: Hall A 6 GeV Transversity experiment coincidence timing spectrum after a cut on the aerogel detector to remove π^\pm .

The kaon identification at the forward-angle will be performed by using the Heavy Gas Čerenkov (HGC) detector and the high-resolution time-of-flight (TOF) information from the MRPC detector. The HGC detector will separate K^\pm from π^\pm in the momentum range from 2.2 GeV/c to 7.0 GeV/c by vetoing the HGC signals during the offline event selection. With reasonable time resolution (e.g. 80 ps), the MRPC's TOF can easily isolate K^\pm from protons up to 6 GeV/c and from π^\pm at low momenta (<3.5 GeV/c). A 50 ps time resolution can reject protons in the full momentum range. With 20 ps time resolution, the MRPC can also distinguish K^\pm and π^\pm up to 7.0 GeV/c. The cross-reference of these two detector systems will also allow us to optimize the PID cuts and evaluate the PID efficiencies. Combining these two detectors we

will effectively detect K^\pm with good efficiency and small pion contamination. A similar method has been proved to be very effective from the Hall A 6 GeV Transversity experiment which used an aerogel Čerenkov detector and scintillator counters for TOF [26].

3.2 Pion rejection by HGC Detector

The HGC uses C_4F_8O/C_4F_{10} gas at a pressure of 1.5 atm and a temperature of 20 °C as the radiator. It works as a threshold detector where the threshold is roughly 2.2 GeV for π^\pm and 7 GeV for K^\pm . The gas length available for Čerenkov light production is about 1 m due to geometrical acceptance constraints and it covers the entire polar angles in the forward-angle region with a full azimuthal coverage. The optical system consists of a ring of 30 spherical mirrors and light reflection cones around PMT assemblies. Each mirror will have a PMT assembly made of 16 Hamamatsu Multi-anode PMTs (H12700) as photon detectors.

The HGC's primary goal would be to provide pion identification with kaon suppression and it relies on placing cuts on the collected number of photoelectrons above the average background level. If we set the threshold reasonably high, we can use the HGC as a veto detector to reject most of π^\pm and thus help kaon identification together with the MRPC's TOF information.

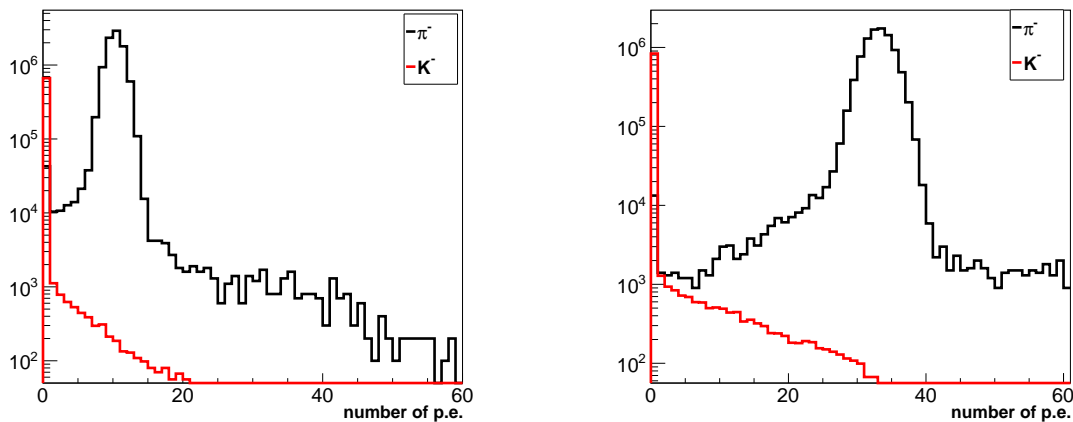


Figure 10: The number of photoelectrons of π^\pm and K^\pm in HGC from 8 deg polar angle at 2.5 GeV (left) and 7 GeV (right) momentum.

We have performed a simplified simulation with the HGC to demonstrate the feasibility. We simulated both negative pion and kaon response of HGC as a part of the whole SoLID-SIDIS ^3He setup. The number of π^\pm is assumed to be 10 times the number of K^\pm . Our simulation only uses π^\pm and K^\pm emitted from the target center and at a polar angle of 8 deg with the momenta of 2.5 GeV and 7 GeV. The 8 deg polar angle is selected because it has shortest radiator length, thus the lowest number of Čerenkov photons a pion will generate and is most difficult to reject. As shown in Figure 10, the π^\pm and K^\pm are well separated while K^\pm show small tails with a very small number of events. This result doesn't include any noise from PMT and DAQ system and there is no integration over a time windows. The overall efficiency of pion suppression will need to be evaluated in a combined study of both HGC and MRPC. If we apply a conservative cut at 5 photoelectrons, we obtain a factor of 100 pion rejection at 2.5 GeV and 400 at 7 GeV.

3.3 Time-Of-Flight PID

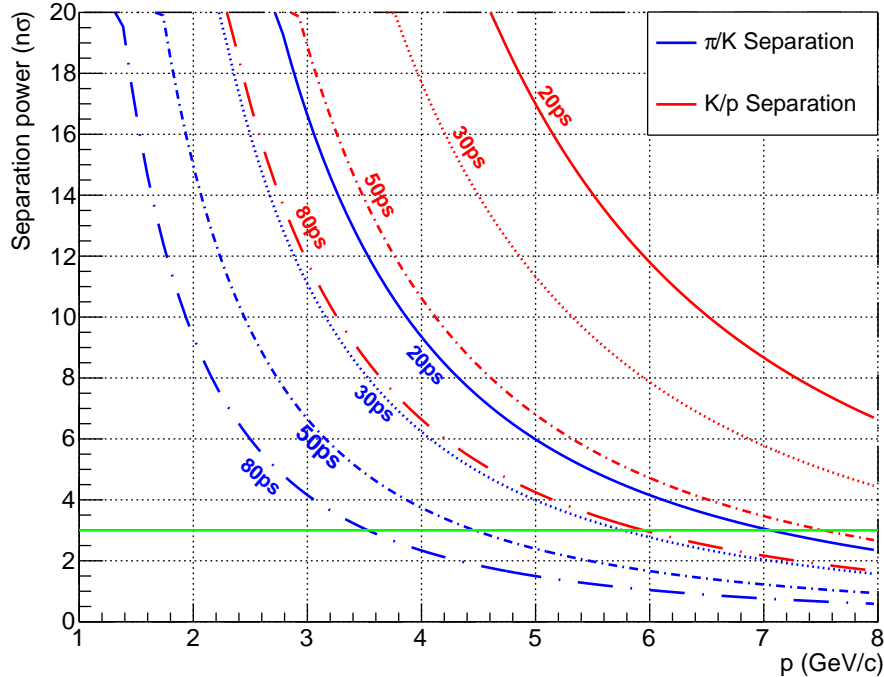


Figure 11: The separation power between π^\pm and K^\pm (blue) and K^\pm and protons (red) as a function of the particle momentum for different time resolutions. The total path length is around 8 m.

While the momenta of charged particles can be determined by reconstructing their tracks traveling in a magnetic spectrometer, the masses (hence the particle types) of these particles can be determined by measuring the TOF after a fixed distance L :

$$m = \frac{p}{c} \sqrt{\frac{c^2 t^2}{L^2} - 1}. \quad (17)$$

Coming from the same location (such as the target), two charged particles with the same momenta but with different masses will have different arrival times when reaching the same detector:

$$\Delta t = t_1 - t_2 \simeq \frac{Lc}{2p^2} (m_1^2 - m_2^2). \quad (18)$$

One can define the separation power of a TOF detector by taking the ratio of the time difference of two particles to the time resolution of the detector:

$$n_\sigma = \Delta t / \sigma_{TOF} \quad (19)$$

For SoLID, the MRPC will be used as the TOF system. Figure 11 shows the separation power of the MRPC with different time resolutions for a total flight distance of 8 m. With a time resolution of 20 ps, one can obtain a 3σ separation between π^\pm and K^\pm up to a particle momentum of 7 GeV/c. Even at the 30 ps level, we still can identify K^\pm up to 6 GeV/c. As shown in Section 4.1, only a small amount of K^\pm have momenta above 6 GeV/c where the HGC is expected to more efficiently separate π^\pm and K^\pm as discussed in the previous section.

3.4 MRPC Detector

The prototype design of the SoLID MRPC is shown in Fig.12. The detector consists of 50 super-modules and each super-module has 3 MRPC modules. There is overlap between modules to avoid the blind area. In each module, there are 10 gas gaps. Each gas gap has a width of 0.25 mm and is separated by 0.7 mm thick glass layers. Tsinghua University has developed a new type of low-resistive glass with the bulky resistivity on the order of $10 \Omega\text{cm}$. The rate capability of this MRPC assembly, with this type of glass, can reach $50 \text{ kHz}/\text{cm}^2$. More details on the MRPC design can be found in the SoLID pCDR [32].

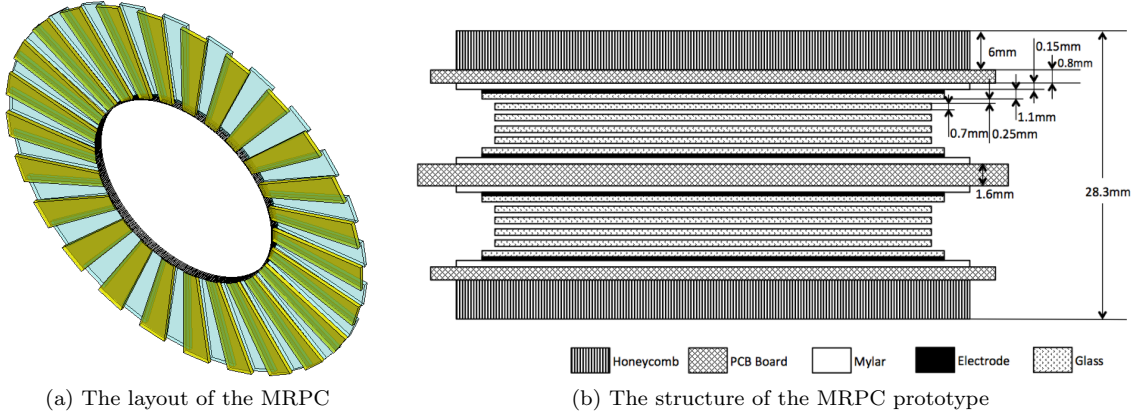


Figure 12: The MRPC prototype design.

The MRPC prototype developed by Tsinghua University has been tested with both cosmic rays and beam [39]. The cosmic test reported an efficiency over 95% and a time resolution around 50 ps with relatively slow front-end electronics. The beam test was performed at JLab utilizing the electron beam during the g2p experiment. The range of particle flux for the beam test was from 1 to $16 \text{ kHz}/\text{cm}^2$. A timing resolution of 80 ps and an efficiency over 94% were obtained even when the flux reached $15 \text{ kHz}/\text{cm}^2$.

3.5 Recent MRPC R&D Progresses

There are two major contributions to the time resolution: the time response of the detector and the performance of front-end electronics. While the time resolution of modern low-noise fast electronics is already very good (only a few pico-seconds), the dominant limitation is from the actual performance of the detector, particularly in a high-rate environment. The ALICE-TOF MRPC reportedly reached 57 ps in the full operation [40] and the ongoing R&D effort is to upgrade the time resolution to be less than 20 ps and also increase the rate capability for the upcoming HL-LHC running. In the last ten years, several R&D works [41, 42] have shown a 20 ps level time resolution on MRPC detectors. The most recent MRPC designed for the ALICE-TOF upgrade showed a time resolution of 16 ps [43]. In the U.S., there is an EIC R&D project (EIC RD2013-5 [44]) to apply the state-of-art time technologies to push the time resolution down to only a few ps for future large-area TOF detector systems including the the next generation MRPC detectors. A thin-gas-gap MRPC prototype developed by members of this collaboration (UIUC and BNL) provided an 18 ps time resolution with the cosmic ray (25 ps at $80\text{Hz}/\text{cm}^2$). Their ongoing R&D effort is also trying to develop a low current, high analog bandwidth preamp for use in fast timing applications.

There has been a joint R&D effort from a Chinese collaboration to develop the next generation MRPC

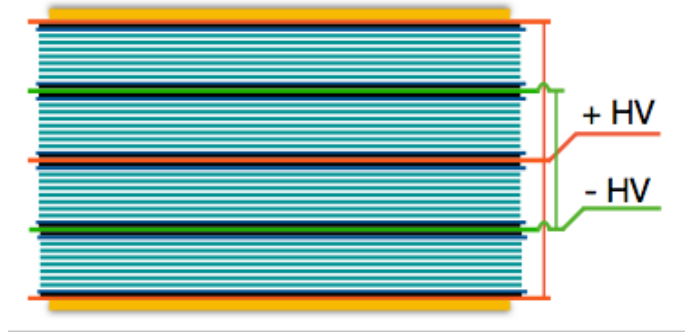


Figure 13: The structure of the testing MRPC at Tsinghua University

for RHIC, SoLID and EIC. In the previous MRPC generations, the signal was read out with NINOs or PADI front-end electronics(FEE) and the time was given with TDC channels. However, the time jitter of the TDC is usually larger than 20 ps and is not suitable for high precision time measurements. The front-end electronics is thus planned to be a fast amplifier and a charge digitizer, in order to take the record of the signal waveform from the MRPC detector.

The MRPC designed for SoLID has a thin gas gap of 104 μm . There are 4 stacks with 8 gaps per stack. A detailed simulation of this MRPC has been made and the waveforms from the FEE was obtained. A time reconstruction method based on the neural network and machine learning algorithms has been developed to take the full use of the information in the signal waveform [45]. The neural network is a powerful tool in solving non-linear pattern recognition problems and has many applications in the fields of not only computer science but also high energy physics as well. In this time reconstruction method, a fully connected network is proposed to learn the waveform patterns from the simulation data and estimate the particle arriving time in the experimental data. The network takes several uniformly distributed points on the leading edge of the signal waveform as the input and outputs the length of the leading edge t_1 . By subtracting t_1 from the peak time t_p , the estimated particle arriving time is $t_a = t_p - t_1$.

A preliminary cosmic ray test was conducted in Tsinghua University with two identical 4×8 gaps MRPCs shown in Figure 13. An amplifier with the bandwidth of 350MHz was used in this test and the waveform digitizer was CAEN DT5742 (based on DRS4-V5 Chip). 8 uniformly distributed points from the leading edge were obtained from the experimental data and feed into the neural network. The network was trained and validated with 120,000 and 50,000 events respectively. Figure 14 shows the time difference of two MRPCs and the time resolution is 27 ps. However, the amplifier used in this test was not fast enough and the digitizers sampling rate was only $\sim 5\text{GHz}$. The case of MRPCs read out with a faster amplifier (signal leading edge $\sim 1\text{ ns}$) and a higher sampling rate ($\sim 10\text{ GHz}$) was simulated. The result shows that the time resolution of about 14 ps can be achieved. Recent studies on the structure of the neural network show that using the Long-Short-Term-Memory network (LSTM) can further improve the time resolution by about 4 ps.

One of the biggest challenges for the SoLID is the tremendous background rates due to the high target luminosities which can certainly make the realistic time resolution worse than the designed performance. Most of the background particles making into the MRPC are low-energy electrons from secondary scattering and can be effectively removed. However, the pile-up effect will dilute the time resolution when many

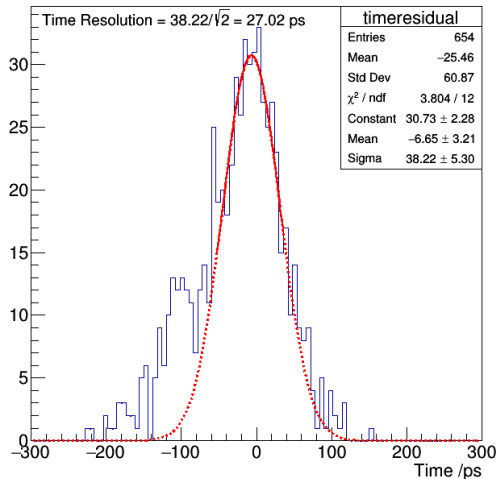


Figure 14: The time difference of two MRPCs at Tsinghua University

background particles come together with good particles into the same detector within the same time-window. Several ongoing MRPC R&D projects aim for sub-picoseconds time resolution in a clean environment and 20 ps or better in high rate environments including the Tsinghua University’s study using the neural network method. In a worse scenario, assuming the actual MRPC time resolution becomes 30 ps under the SoLID high-rate environment, we still can use the TOF to separate K^\pm from π^\pm up to around 6 GeV/c above which the event rate is already very low and the lose of kinematic phase-space is small (as shown in Fig. 24 in Section 4.1). Meanwhile, the HGC with veto signals can more effectively suppress π^\pm at high momenta. Despite the challenge, we are still confident that the current R&D efforts will reach the timing resolution requirement of this experiment before the running of SoLID.

3.6 MRPC Simulation Framework

To study the detector performance and design optimization, it is desired to have a digitization software. The SoLID detector simulation is done with a GEMC Geant4 based software. A standalone post-GEMC simulation software has been developed to optimize the MRPC design. Together with GEMC it simulates physics processes of the MRPC as well as reconstructing time using the induced signal current. Like other gaseous detectors, the main physics process of the MRPC is based on ionization. When a charged particle passes through a gas volume, it ionizes gas atoms which can result in electron-ion pair production. A primary electron with enough energy can further ionize other atoms. In a very high electric field, it can create an electron avalanche and induce a signal on the electrodes.

Figure 15 shows an overview of the simulation procedure. The output of the GEMC simulation provides information on the physics hits. The detector response is characterized by transport parameters such as Townsend (avalanche) coefficient α , attachment coefficient η and electron drift velocity v . The parameters are obtained using the MAGBOLTZ program for an operating voltage of 6.6 kV which gives $E = 108$ kV/cm. For the SoLID MRPC simulation we used the following parameters: $\alpha = 129/\text{mm}$, $\eta = 5.435/\text{mm}$, and $v = 0.201$ mm/ns.

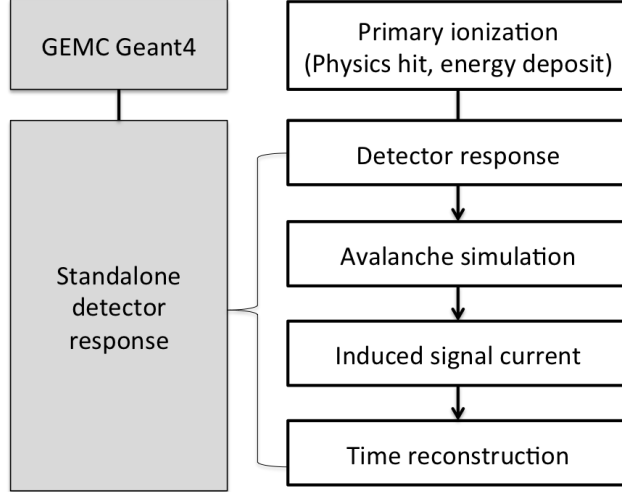


Figure 15: Schematic of the MRPC simulation

The electron multiplication (avalanche) process is simulated using a 1-Dimensional avalanche gas model developed by W. Riegler, C. Lippmann, and R. Veenhof [46]. The model allows an efficient avalanche simulation. In the simulation, an electron starts an avalanche that will grow until they reach to the end of the gas gap. Considering an electron at a position x in an gap, one can calculate the probability for an avalanche started with a single electron to contain n electrons at $x+dx$ as:

$$P(n, x) = \begin{cases} k \frac{\bar{n}(x)-1}{\bar{n}(x)-k} & (n=0) \\ \bar{n}(x) \left(\frac{1-k}{\bar{n}(x)-k} \right)^2 \left(\frac{\bar{n}(x)-1}{\bar{n}(x)-k} \right)^{n-1} & (n>0) \end{cases}$$

where the average number of electrons is $\bar{n}(x) = e^{(\alpha-\eta)x}$, and $k = \eta/\alpha$. For each gas layer, the gap is divided into 200 steps, and for each step dx , the number of electrons with a probability for ionization and attachment is calculated. The same process is repeated over all electrons within a given gap until they reach to the end of the gap. In addition, we employ an effective model based on the central limit theorem once the number of electrons is sufficiently large ($n > 200$) in order to reduce computing time. In such a case, the number of electrons at $x + dx$ can be obtained by sampling a random number from a Gaussian with a mean of $\mu = n\bar{n}(dx)$ and $\sigma = \sqrt{n}\sigma(dx)$. Note that this 1-D model does not take into account that the growth of the avalanche is affected by space charge. The space charge effect stops exponential avalanche growth. In this simulation, we take the space charge effect into account by applying a simple cut-off to the avalanche size. Once the number of electrons exceeds $1.5 \cdot 10^7$, the avalanche size will be saturated as shown in Fig. 16. As it can be seen from panel b we obtain a very reasonable agreement between the simulation and the effective model.

The induced current signal is then calculated using Ramo's theorem [47]:

$$i(t) = E_w \cdot v \cdot e_0 \cdot N(t) \quad (20)$$

where E_w is the weighting electric field, v is the electron drift velocity, e_0 is the electron charge, and $N(t)$ is the number of electrons at time t . The weighting field is calculated using the number of gas gaps, the width

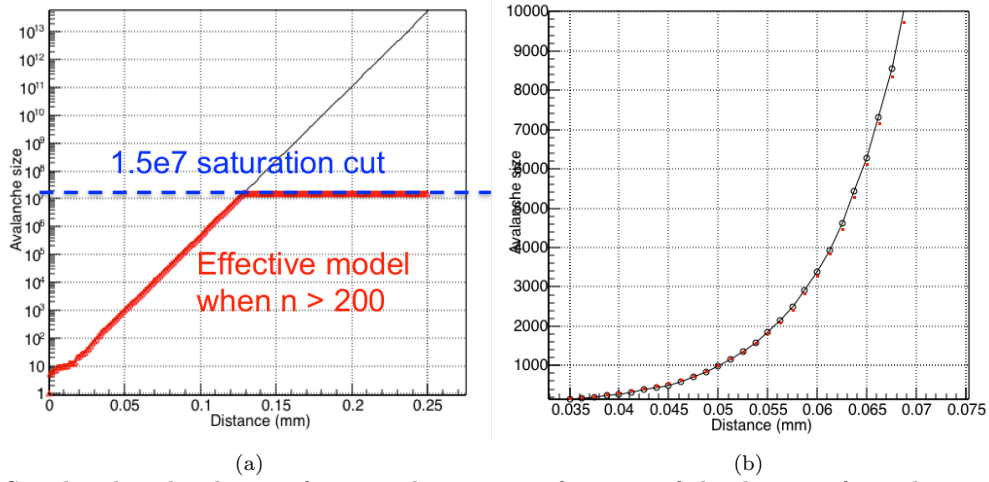


Figure 16: Simulated avalanche size from an electron as a function of the distance from the entrance of the gap for (a) the full gap width and (b) a zoomed-in for a region close to the entrance of the gap. Black circles show the simulated avalanche size, and the red circles show the avalanche size from the effective model when $n > 200$. The blue dashed line shows a saturation cut-off.

of gaps and other material plates, and permittivity of the resistive plates. Lastly, the timing information is obtained using a leading edge discriminator.

In addition to the gas transport parameters, the simulation is further tuned to match with the cosmic test result. A Gaussian noise in the signal processing is introduced with σ_{noise} , and an additional smearing factor for the timing of σ_{smear} are applied to match the simulation output with the data. Both the time and integrated charge are recorded for each particle that enters the MRPC volume. The time-walk correction is then performed to get the timing resolution. The time-walk correction function used can be defined as:

$$f(Q) = c_0 + \frac{c_1}{\sqrt{Q}}. \quad (21)$$

Figure 17 (c) shows a time distribution after the time-walk correction from a single muon simulation. The resolution of about 49 ps is obtained in the simulation which is similar to the one from the cosmic test with the prototype design.

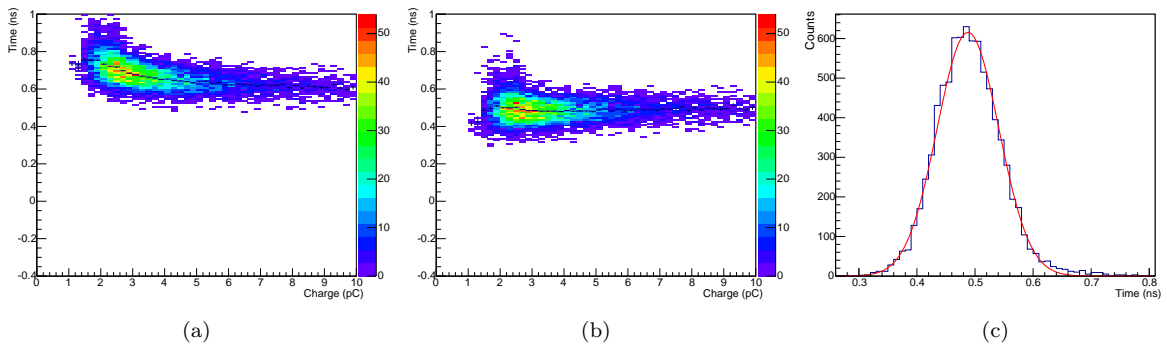


Figure 17: Time-charge correlation: (a) before time-walk correction and (b) after the correction. (c) Timing distribution after time-walk correction. The obtained time resolution from a Gaussian fit is ≈ 49 ps.

3.7 Kaon Identification with TOF and HGC

Using the simulation software, preliminary studies have been performed for π^\pm and K^\pm . In this study, single K^- and π^- were generated for various momentum settings. The smearing factor is adjusted in the simulation in order to set the time resolution to ~ 20 ps. The average π^-/K^- ratio estimated using the SIDIS MC (see Section 4.2 for details) is around 10. The ratio is larger at low momenta, but the pion rate drops more quickly as the momentum increases. The ratio reduces to around 3 at the momenta of 4-6 GeV/c. The HGC can further reduce the pion rates by vetoing pion signals at momenta above its threshold as discussed in Section 3.2. In the simulation study, the pion yield is scaled according to the reduced π^-/K^- ratio. From the kaon Δt ($= t_{MRPC} - t_{expected}^{kaon}$) distribution the peak and sigma values are extracted, and a $\pm 3\sigma$ TOF cut is applied to estimate the pion contamination.

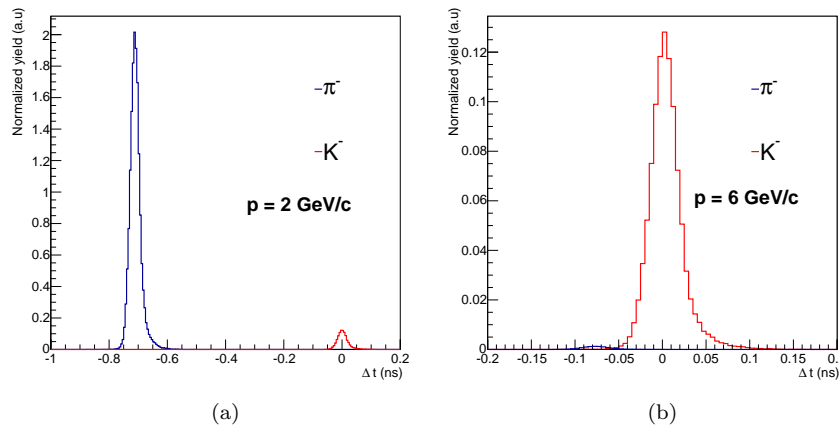


Figure 18: Time difference distributions between the MRPC time and the expected Kaon signal time for the momentum of 2 GeV/c (left) and 6 GeV/c (right). The time resolution of 20 ps is assumed. The pion yields are scaled using the expected π^-/K^- ratio and pion rejection factor from the HGC. The total scale factors of 16 and 0.01 are used for 2 GeV/c and 6 GeV/c, respectively.

Figure 18 shows simulated Δt distributions for momenta of 2 and 6 GeV/c. For 2 GeV/c where the momentum is below the pion Čerenkov threshold (~ 2.2 GeV), we scaled the pion yield by the π^-/K^- ratio of 16 that is estimated by the SIDIS MC. At this momentum, the MRPC can separate K^\pm from π^\pm very well as shown in Fig. 18 (a). The MRPC even with an 80 ps time resolution can provide enough separation power at this momentum. At higher momenta, it is important to suppress the pion background due to relatively limited separation power of the TOF. Assuming the HGC reduces $\pi^- : K^-$ to 1:100 at the momentum of 6 GeV/c and the time resolution of 20 ps, the pion contamination is estimated as $\sim 0.1\%$ from Fig. 18 (b). For the time resolution around 30 ps, the pion contamination would still be less than 1% for high momentum region (4-6 GeV/c) without taking into account other background effects.

As discussed in section 3.5 there have already been several MRPC detector designs that have demonstrated a timing resolution below 20ps. Together with the detailed studies performed at Tsinghua University we plan to use the simulation framework described above to cross-check results and guide future detector design. A detailed simulation is currently underway and will produce results in the near future for the updated MRPC. The final detector design will take into consideration realistic high-rate background effects.

4 Projected Results

The kinematic coverages and projected results were produced based on exactly the same detector setup of the transversely polarized ^3He target experiment (E12-10-006 [19]) and the transversely polarized proton target experiment (E12-11-108 [20]). We also applied the same target luminosities and the approved beam-time. As discussed in Section 3, a time resolution of 20 ps should allow us to separate K^\pm from π^\pm up to a maximum momentum of 7 GeV/c . To be shown later, the maximum momentum of K^\pm in the SIDIS reaction at 11 GeV is about 7.5 GeV/c without the $0.3 < z < 0.7$ cut (and becomes 6.5 GeV/c with the z cut). It means that the requirement on the timing resolution should be sufficient.

The Monte-Carlo generator used in this study is the updated version of our standard SIDIS generator which has been widely used in the original three SoLID-SIDIS proposals, the SoLID pCDR [32], and our Transversity projection paper [48]. We have updated the unpolarized SIDIS cross section model [49] using the CJ15 PDF sets [50] and DSS LO Fragmentation Functions [51]. While the older model in this generator was fine-tuned using the 6 GeV Hall A pion transversity data, this new model gives better agreement with the HERMES results and provides a better estimation of the K^\pm production. Note that the following kinematic cuts were applied when generating the simulated events to only select DIS events: $Q^2 > 1 \text{ GeV}^2$, $W > 2.3 \text{ GeV}$, and $W' > 1.6 \text{ GeV}$.

4.1 Kinematic Coverage

Following our conventional way of performing the SIDIS simulation, we produced the SIDIS events uniformly in a kinematic phase-space which is slightly wider than the actual designed range, then calculated the weight of each event based on its unpolarized cross section normalized by target luminosities and approved beam-time. The event-by-event weight was further folded in the acceptance probabilities of the electrons and K^\pm in this event. The most updated detector acceptance profiles using the CLEO-II solenoid magnet were created from our GEMC simulation. Fig. 19, Fig. 20 and Fig. 21 show the acceptance of electrons and K^\pm in both the NH_3 and ^3He configurations, respectively. Note that for the NH_3 setup, there are certain regions where the rates are very high due to the "sheet of flames" issue caused by the interference between the strong DNP target magnet field and the solenoid magnet field. The detectors in these regions are disabled and that causes the gaps in the azimuthal angular coverage.

The kinematic coverage of the Kaon-SIDIS production are shown in Fig. 22 and Fig. 23. As discussed in the previous section, the maximum momentum range of K^\pm can be affected by the time resolution of the MRPC. Fig. 24 shows that when $P_K > 6 \text{ GeV}/c$ the correlations between kaon momenta and important physics quantities, Q^2 , z , p_T and x_B , are less important, so the effect will be minimum if a worse time resolution (30 ps) forces us to cut out these physics regions.

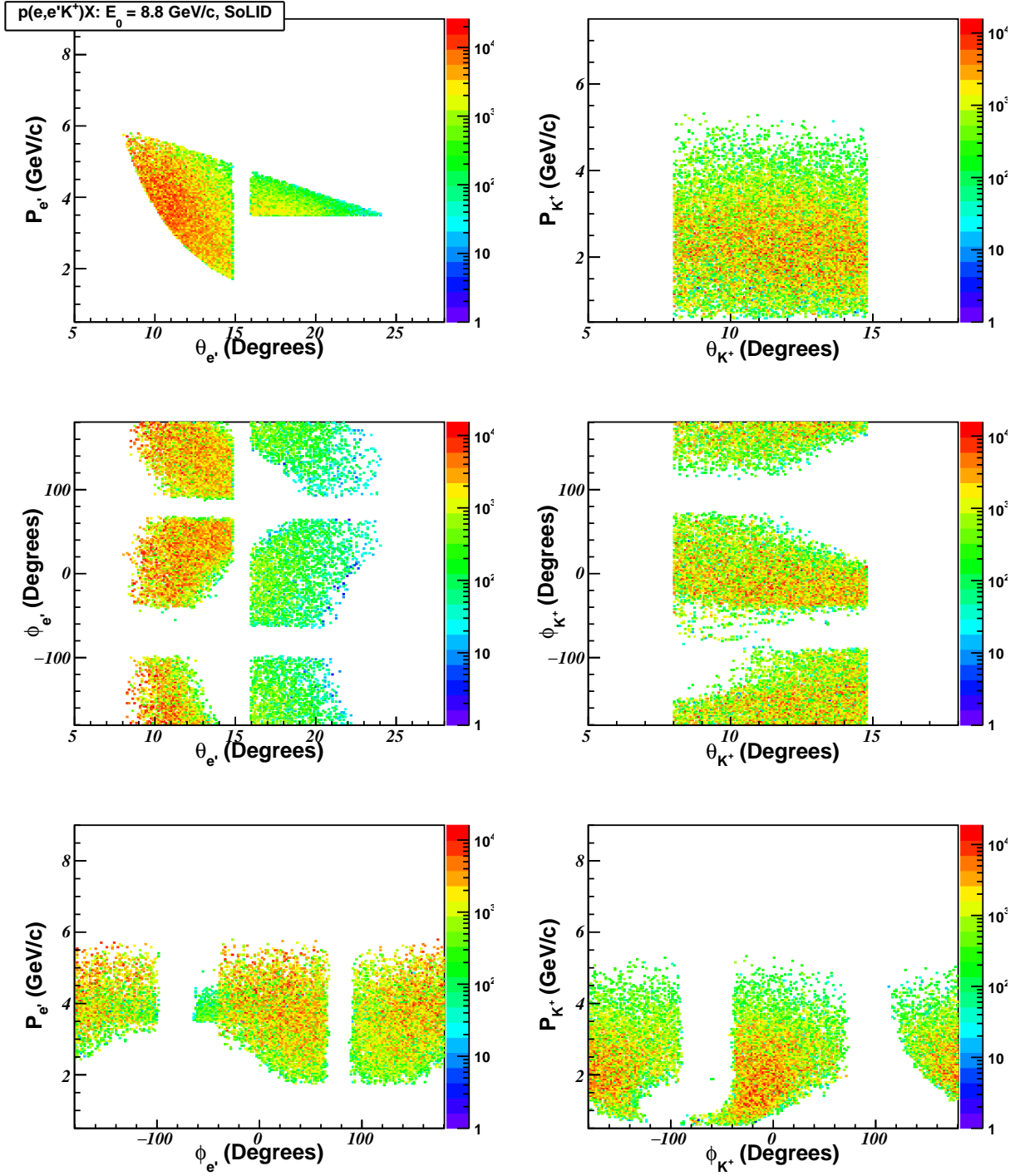


Figure 19: The acceptances of electrons and K^+ from the SIDIS reaction at 8.8 GeV using the NH_3 target and the SoLID (simulated by GEMC). The gaps in ϕ_{e^+} and ϕ_{K^\pm} are the cut-off regions where the 5T transverse NH_3 target magnet field and the 1.4T longitudinal solenoid magnet field create high background in narrow bands of azimuthal angles.

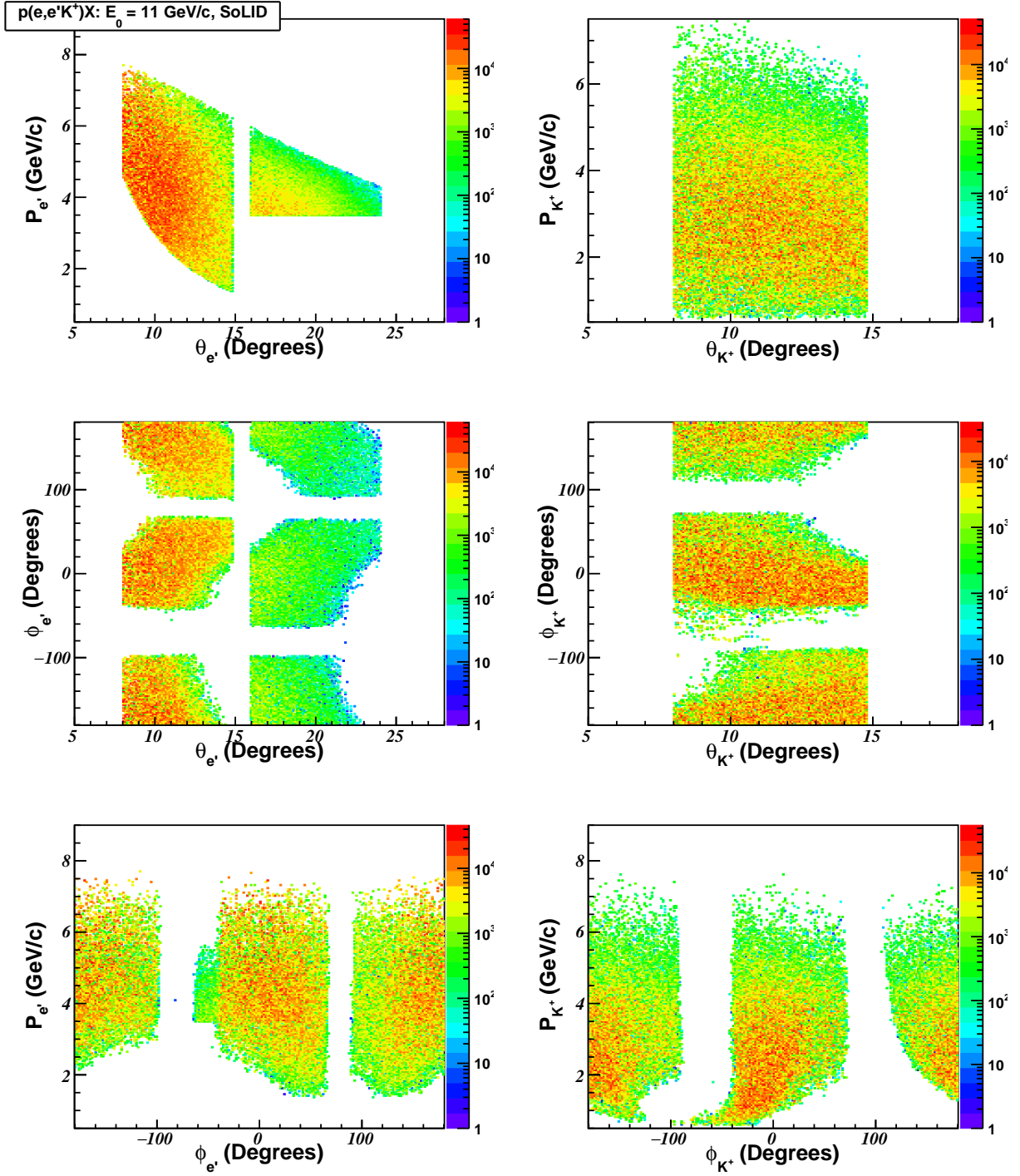
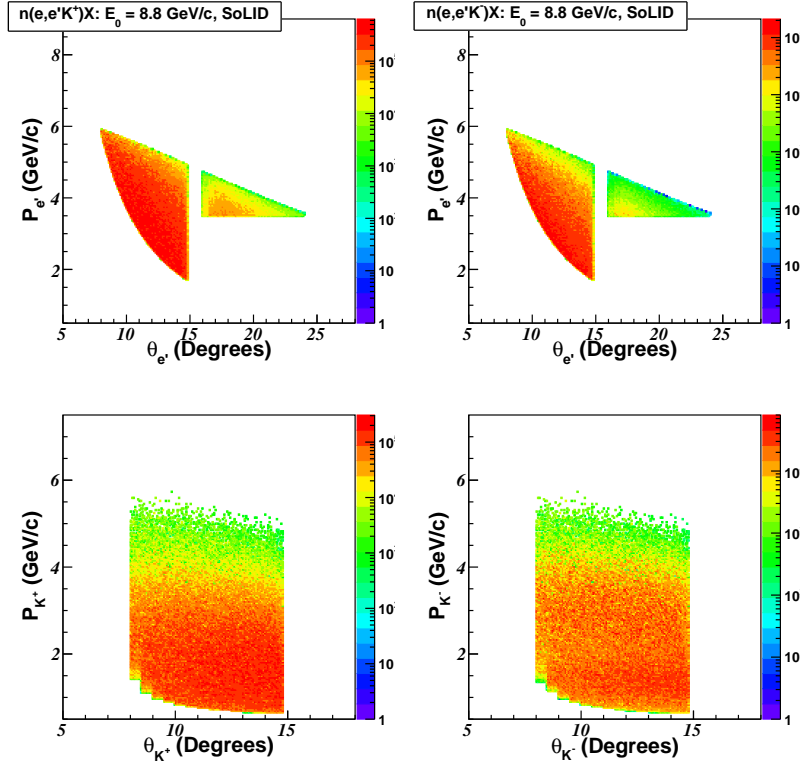
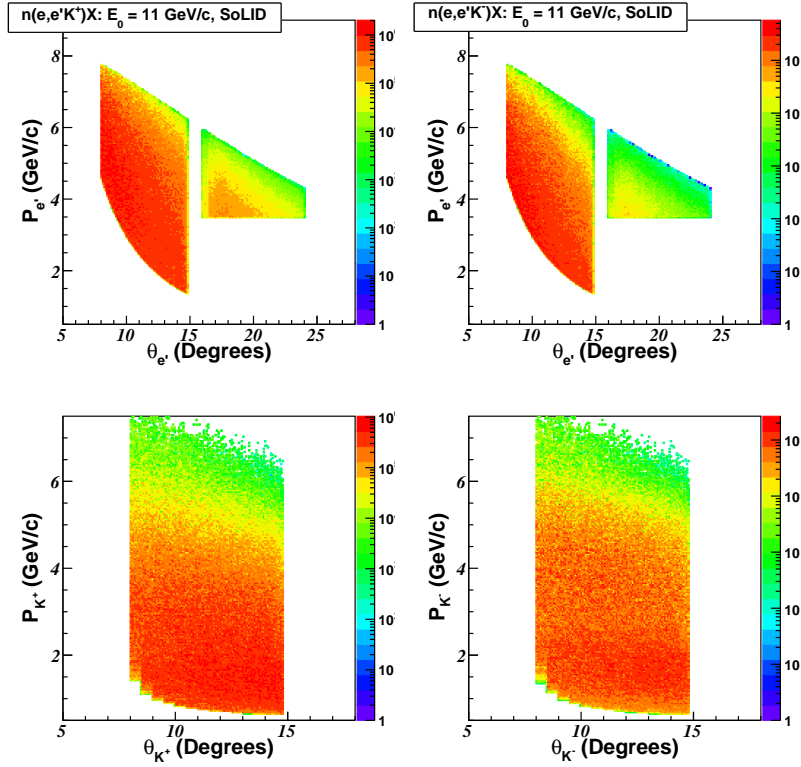


Figure 20: The acceptances of electrons and K^+ from the SIDIS reaction at 11 GeV using the NH_3 target and the SoLID (simulated by GEMC). The gaps in $\phi_{e'}$ and ϕ_{K^\pm} are the cut-off regions where the 5T transverse NH_3 target magnet field and the 1.4T longitudinal solenoid magnet field create high background in narrow bands of azimuthal angles.

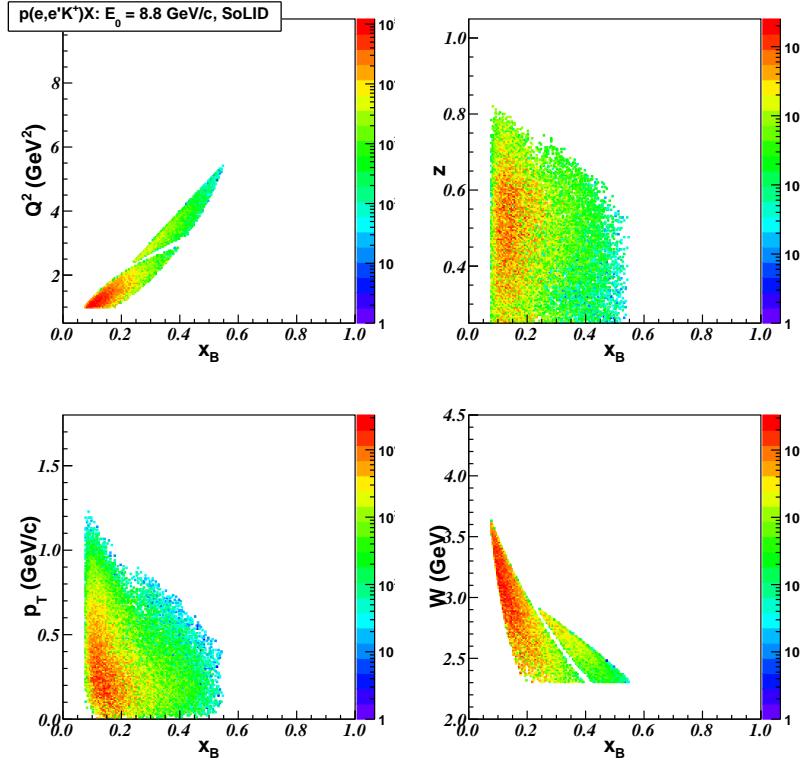


(a) $E_0 = 8.8$ GeV

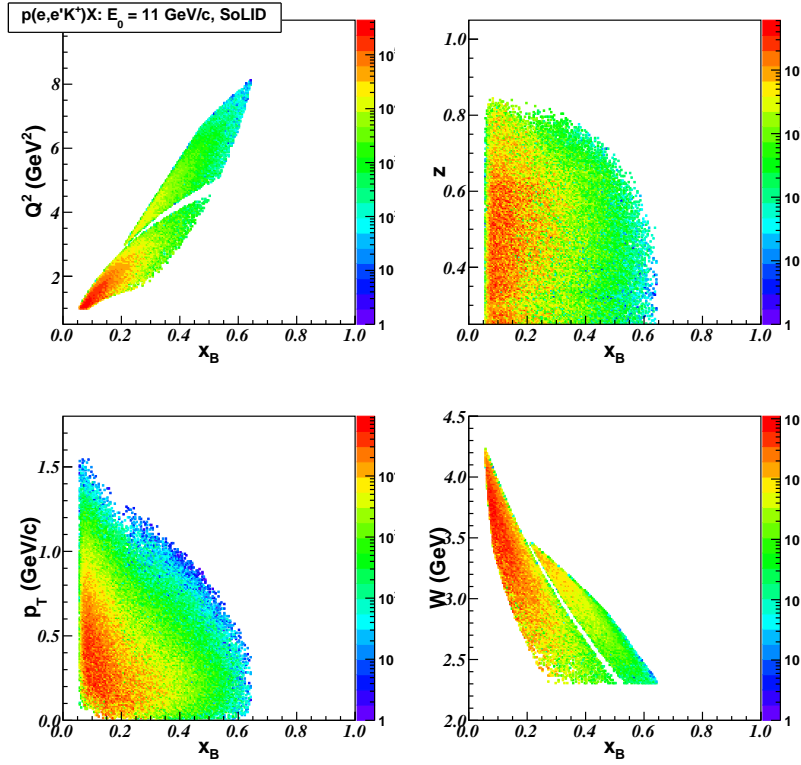


(b) $E_0 = 11$ GeV

Figure 21: The acceptances of electrons and K^+ from the SIDIS reaction: at 8.8 GeV (top) and 11 GeV (bottom) using the ^3He target and the SoLID (simulated by GEMC).

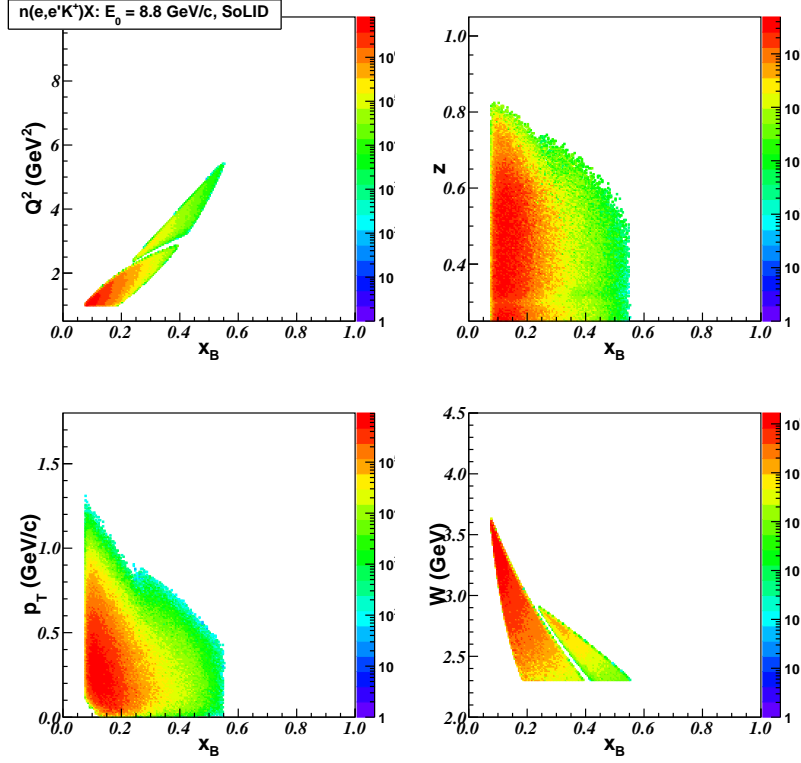


(a) $E_0=8.8$ GeV

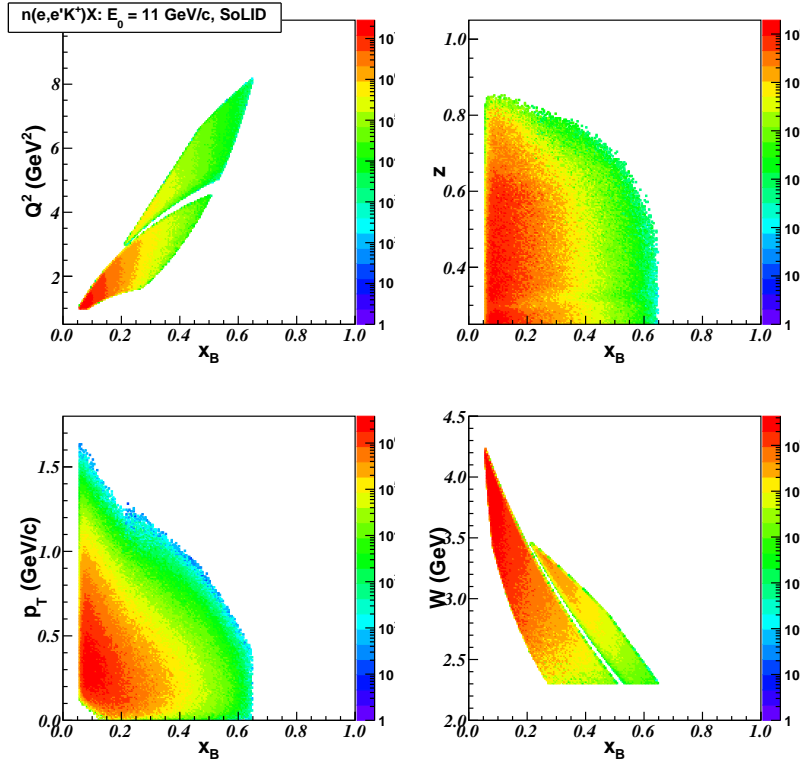


(b) $E_0=11$ GeV

Figure 22: The kinematic coverage of the Kaon-SIDIS production with the NH₃ target and the 8.8 GeV (top) and 11 GeV (bottom) electron beam.



(a) $E_0=8.8 \text{ GeV}$



(b) $E_0=11 \text{ GeV}$

Figure 23: The kinematic coverage of the Kaon-SIDIS production with the ^3He target and the 8.8 GeV (top) and 11 GeV (bottom) electron beam. Unlike the NH_3 setup, the ^3He setup provides a full coverage of the azimuthal angles for both $\phi_{e'}$ and ϕ_{K^\pm} .

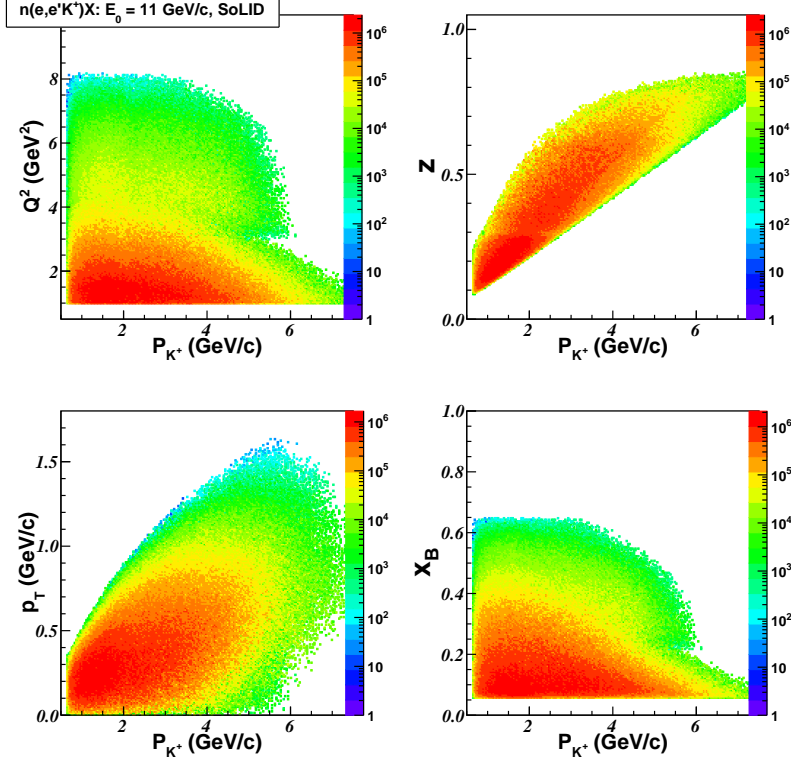


Figure 24: The correlations of K^\pm momenta vs important physics quantities using the ^3He target at 11 GeV.

4.2 Rate Estimations

SoLID-SIDIS Coincident Rates (Hz)				
Polarized Target	^3He ("n")		NH_3 ("p")	
Beam Energy	8.8 GeV	11 GeV	8.8 GeV	11 GeV
e-(FAEC+LAEC)+ K^+ (FAEC)	359.3	575.6	4.9	10.4
e-(LAEC+LAEC)+ K^- (FAEC)	83.2	144.1	0.93	2.7
e-(FAEC+LAEC)+ π^+ (FAEC)	1555.0	2185.9	20.3	37.4
e-(LAEC+LAEC)+ π^- (FAEC)	1012.5	1449.6	10.2	20.7

Table 1: Estimated Rates of the Kaon-SIDIS production with ^3He (neutron) and NH_3 (proton) targets at 8.8 GeV and 11 GeV beam energies. The pion rates are also given here as comparison.

The rate estimation was performed using the SIDIS MC events weighted by the unpolarized kaon cross sections, target luminosities, and the SoLID-SIDIS acceptance profiles. We used the designed target luminosity of $1 \cdot 10^{35} \text{ cm}^{-1} \text{ s}^{-1}$ per target for NH_3 and $1 \cdot 10^{36} \text{ cm}^{-1} \text{ s}^{-1}$ per target for ^3He , respectively. A cut, $0.3 < z < 0.7$, was applied in addition to the kinematic cuts mentioned above. As a comparison and a cross check, the pion rates are also listed here which were calculated with the same generator and the same procedure. The pion rates are consistent with our previous estimations in the SoLID pCDR [32] where we used an older cross section model.

4.3 Projected Asymmetries

We combined the 8.8 GeV and 11 GeV simulation data together and used the corresponding approved beam-time of the pion measurements with both polarized targets. We then binned the data in terms of 4D (Q^2 , z , P_{hT} , x_B) and calculated the statistical uncertainties of the K^\pm measurements. The procedure of binning the data and calculating numbers of events in each bin is identical to the one used in obtaining the most updated projection results of the pion measurements. The main differences are the models that calculate kaon unpolarized cross sections. We also used the more up-to-date detector acceptance profiles. On the other hand, since the K^\pm rates are much lower than the pion's, we had to enlarge the bin sizes of Q^2 , z and p_T , which are now defined by the following:

$$Q^2 \text{ bins}[3] = (1.0 - 2.0), (2.0 - 4.0), (4.0 - 10.0), \text{ in GeV}^2, \quad (22)$$

$$z \text{ bins}[4] = (0.3 - 0.4), (0.4 - 0.5), (0.5 - 0.6), (0.6 - 0.7), \quad (23)$$

$$P_{hT} \text{ bins}[5] = (0.0 - 0.2), (0.2 - 0.4), (0.4 - 0.6), (0.6 - 1.0), (1.0 - 1.6), \text{ in GeV}/c. \quad (24)$$

The way to determine the x_B -bins is the same as the one in the pion measurements where we require the maximum statistical error in each bin to be $\leq 5\%$. The experimental observable of this measurement is the single spin asymmetry (SSA) with an unpolarized electron beam and transversely polarized target, which is defined as:

$$A_{UT}(Q^2, z, p_T, x_B, \phi, \phi_S) = \frac{1}{f_d P_t} \cdot \frac{N^\uparrow - N^\downarrow}{N^\uparrow + N^\downarrow}, \quad (25)$$

where $N^{\uparrow(\downarrow)}$ corresponds to the number of events with the target spin orientation in two opposite directions, (e.g., up (down)). f_d is the dilution factor calculated bin-by-bin using our model as being used in our previous pion SIDIS proposals, and P_t is the polarization of the target. For protons in NH_3 , f_d is roughly 0.13 and P_t is set to be 70%. For neutrons in ^3He , f_d is between 0.15 to 0.3 and P_t is 65% \cdot 86.5%. Note that during the projection study we set A_{UT} to be constantly zero for all bins since their amplitudes are small and not well determined theoretically and experimentally. We are interested in the relative statistical uncertainty of each bin which is defined as: $\delta A_{UT} = 1/\sqrt{(N^\uparrow + N^\downarrow)/2}$. Let's define $N = (N^\uparrow + N^\downarrow)/2$ as the number of events with unpolarized (or spin-average) target orientation, then in our simulation, we can calculate its value for each (Q^2 , z , p_T , x_B) bin:

$$N = \left(\sum_{i \in \text{bin}} \sigma_i^{avg} \cdot Acc_i^{(e'+K^\pm)} \right) \cdot PSF/N_{gen} \cdot T_{8.8\text{GeV}(11\text{GeV})} \cdot Lumi \cdot \epsilon_{det,eff}, \quad (26)$$

where σ_i is the unpolarized SIDIS cross section per target, $Acc_i^{(e'+K^\pm)}$ is the product of the electron acceptance and K^\pm acceptance in SoLID. They vary event-by-event. PSF and N_{gen} are the total phase-space and the number of total generated MC events defined in the GetSIDIS generator. $T_{8.8\text{GeV}(11\text{GeV})}$ is number of the approved beam-time (in seconds) on NH_3 or ^3He targets at 8.8 GeV or 11 GeV electron beam energy. $T_{8.8\text{GeV}} = 29$ days and $T_{11\text{GeV}} = 56.5$ days for NH_3 , and $T_{8.8\text{GeV}} = 21$ days at and $T_{11\text{GeV}} = 48$ days for ^3He . $Lumi$ is the luminosity of the targets and their numbers can be found in Section 4.2. $\epsilon_{det,eff}$ is the total detector efficiency of detecting electrons and kaons which are set to be 85%, respectively.

With the real experimental data, we can further decompose the SSA into different modules with different

azimuthal angular dependences which correspond to different TMD contributions as discussed in Section I:

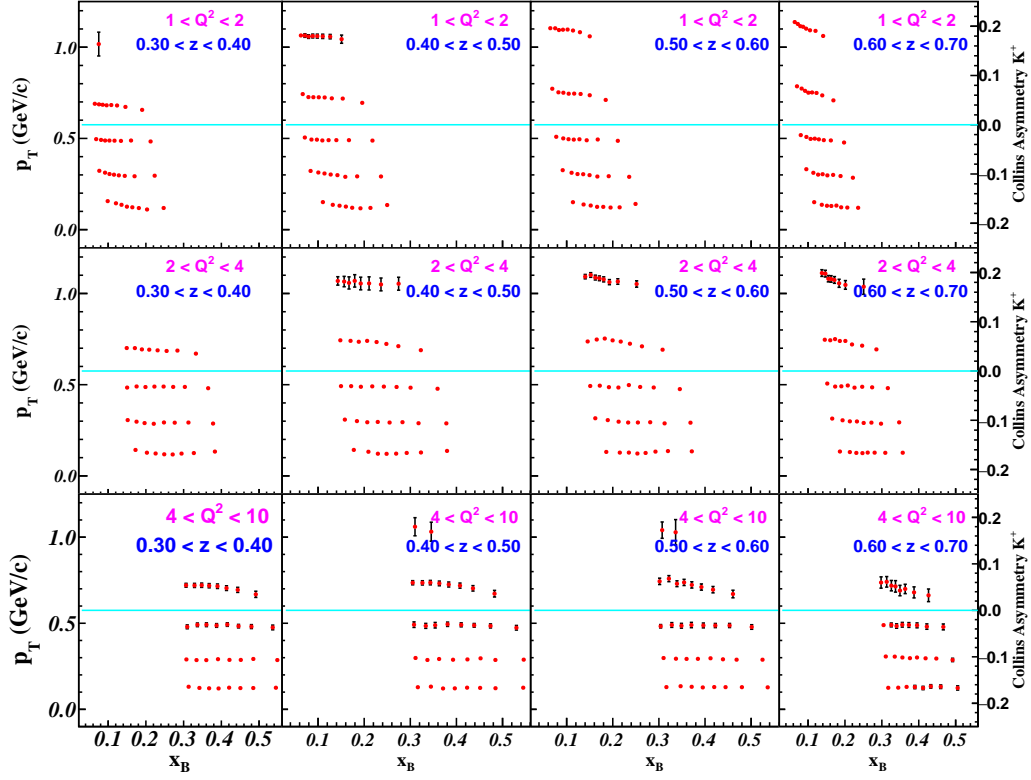
$$A_{UT} = A_{UT}^{Collins} \sin(\phi + \phi_S) + A_{UT}^{Sivers} \sin(\phi - \phi_S) + A_{UT}^{Pretzelocity} \sin(3\phi - \phi_S) + \dots, \quad (27)$$

In this projection, we also estimated the effect of the incomplete azimuthal angular coverage to the total uncertainties when extracting Collins, Sivers, and Pretzelocity asymmetries. The full 4π coverage of the SoLID detector results in this effect to be mostly at few percentage levels for the ^3He setup while it can be slightly larger for the NH_3 setup due to the azimuthal gaps. The effect only becomes large at certain kinematic regions where the azimuthal angles are partially covered. The impact of this effect was added as a correction factor for each bin on top of the bin-by-bin statistical uncertainty when presenting uncertainties of individual asymmetries. The projected results are given in Fig. 25 for extracting the Collins K^\pm asymmetries for the ^3He target. The results for the Sivers asymmetries are similar as shown in Fig. 26. We totally obtained near 430 bins in 4D with uncertainties mostly less than 1% thanks to the higher target luminosity. Some high p_T points have significantly large error bars due to the large correction factors (up to 3) for limited azimuthal angular coverage. The uncertainties for the NH_3 setup, especially for K^- , are much larger under the 4D binning due to the low production rates. We integrated over the Q^2 range and only performed the 3D (z, p_T, x_B) binning, as shown in Fig. 27 and Fig. 28. We obtained roughly 120 bins in 3D with most uncertainties less than 5%. The projected coverage and uncertainties are greatly improved compared with the HERMES and COMPASS data. They are also significantly better than the CLAS12 proposal (C12-11-111 [22]) which only binned in 2D (p_T, x_B). During the real data analysis, the binning methods on both targets can be systematically optimized based on the actual rates and acceptance.

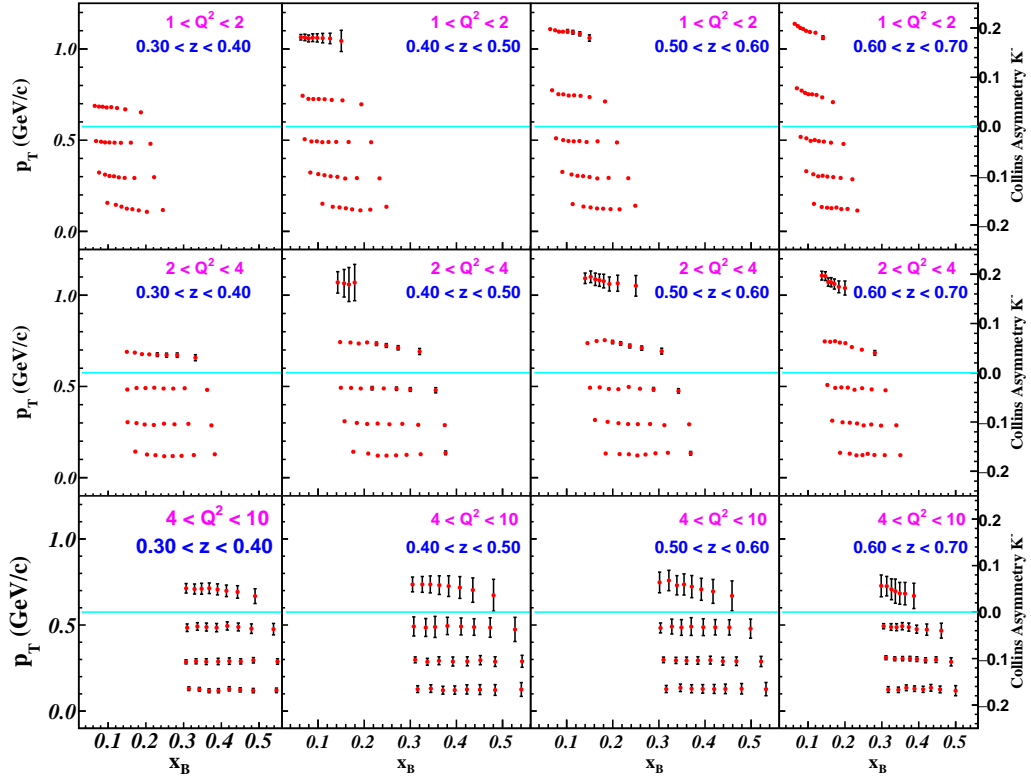
The projection of the Pretzelocity asymmetry is not shown here. The model prediction of the pion Pretzelocity asymmetry is only at the level of sub-percentage, and hence we had to bin the data only in the x_B dimension to obtain the statistical uncertainties at such level. Because the prediction of the kaon Pretzelocity asymmetry is yet available, any projection won't be useful, especially due to the very low K^\pm production rates. However, during the real data analysis, we will still extract this asymmetry together with other asymmetries and study its actual amplitude.

We would like to stress that the total SSA in Eq. 25 (or Eq. 27) are our major experiment observables and for now we don't attempt to make any direct connections to individual TMDs. As discussed in Section 1.4, a theoretical model suggests that only 20% of our SoLID kaon data are under the current fragmentation region. We require a cleaner theoretical definition of the kaon fragmentation region when the future data become available for the TMD extraction.

In the approved SoLID-SIDIS proposal [19, 20, 33], the measurement of double spin asymmetries (DSA) in the π^\pm production was also proposed with an additional requirements on the longitudinally polarized electron beam and the both longitudinally and transversely polarized targets. The π^\pm DSA asymmetries are related to other TMD functions such as the Helicity TMD (g_{1L}) and two Worm-Gear TMDs (g_{1T} and h_{1L}^\perp) which provide unique sensitivity to the orbital angular momentum (OAM) of valence-quarks. Although in this proposal our main physics goal is to extract the K^\pm Collins, Sivers and Pretzelocity asymmetries using transversely polarized targets, we leave the opportunity open to also measure the DSA in K^\pm production with both transversely and longitudinally polarized targets to study the OAM of sea quarks. The work can be a standalone run-group proposal in the near future or can be carried out simultaneously with this proposed measurement.

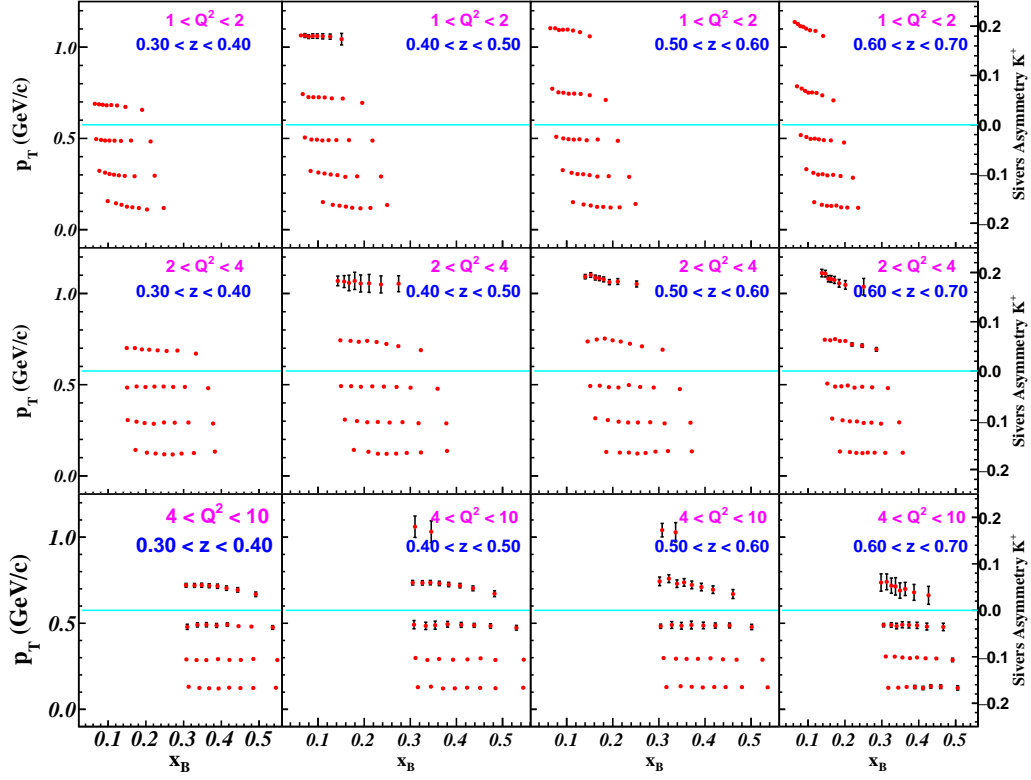


(a) $\bar{n}(e, e' K^+)X$

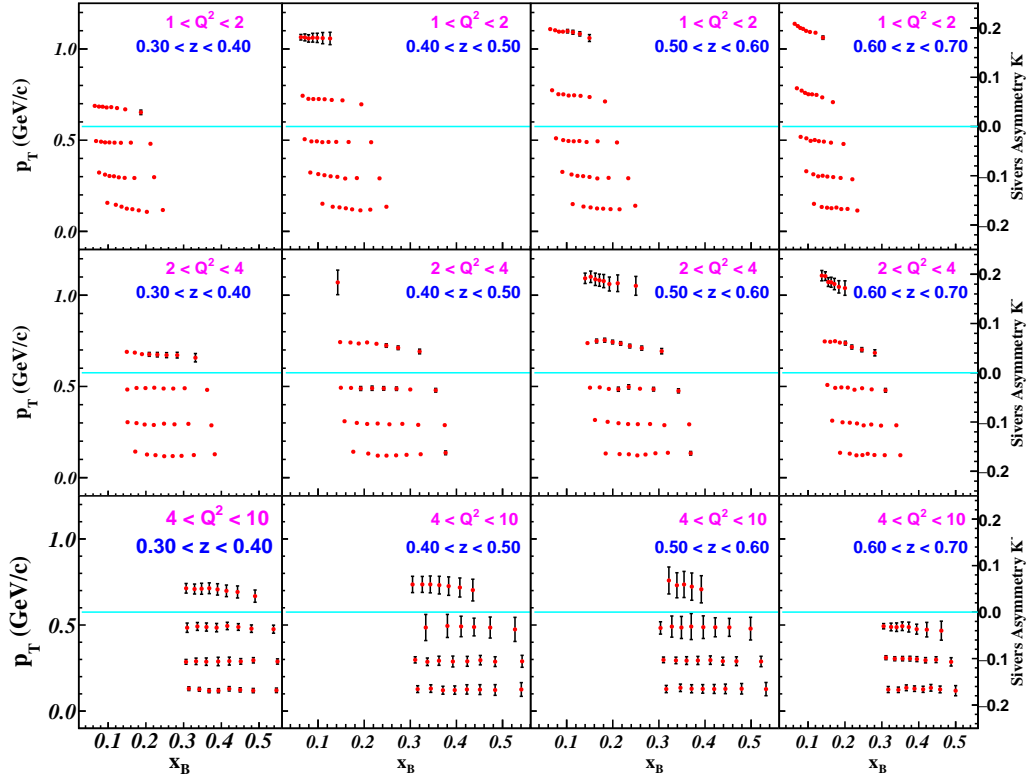


(b) $\bar{n}(e, e' K^-)X$

Figure 25: The 4D (Q^2, z, p_T, x_B) binning projection and statistical uncertainties of the K^\pm Collins asymmetry ($A_{UT}^{\sin(\phi+\phi_S)}$) for the transversely polarized ^3He (neutron) target after combining the 11 GeV and 8.8 GeV simulation data. The sizes of the uncertainties are indicated by the Y axis on the right.

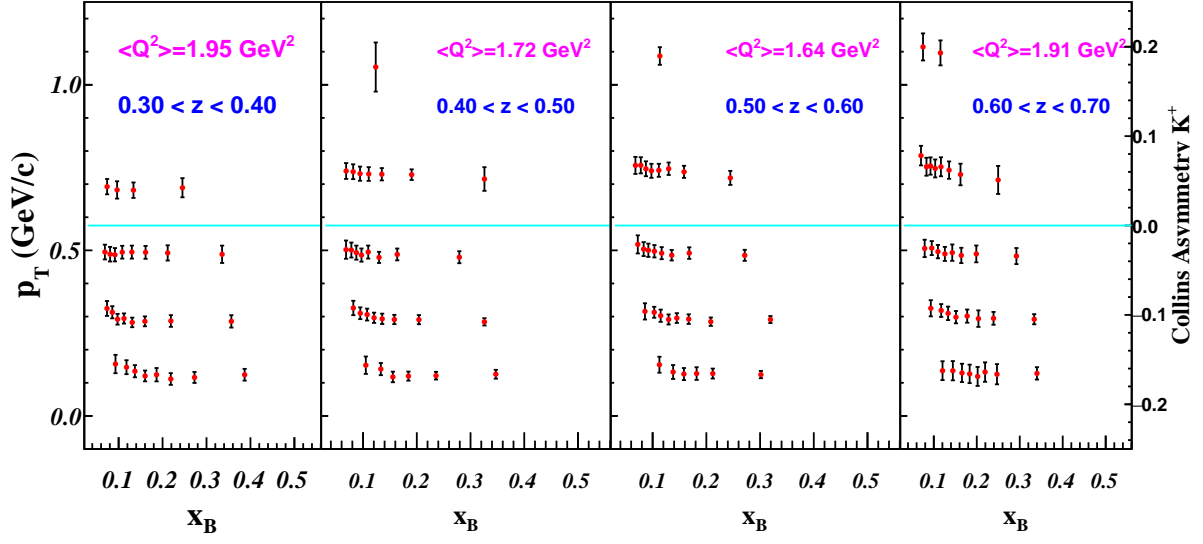


(a) $\bar{n}(e, e' K^+) X$

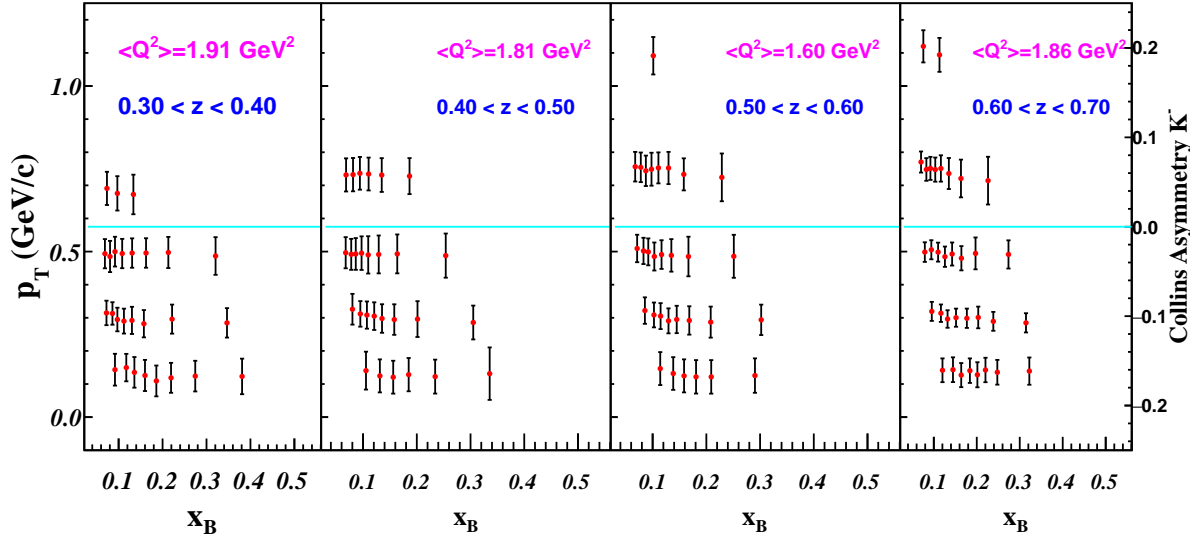


(b) $\bar{n}(e, e' K^-) X$

Figure 26: The 4D (Q^2 , z , p_T , x_B) binning projection and statistical uncertainties of the K^\pm Siverts asymmetry ($A_{UT}^{\sin(\phi-\phi_S)}$) for the transversely polarized ^3He (neutron) target after combining the 11 GeV and 8.8 GeV simulation data. The sizes of the uncertainties are indicated by the Y axis on the right.

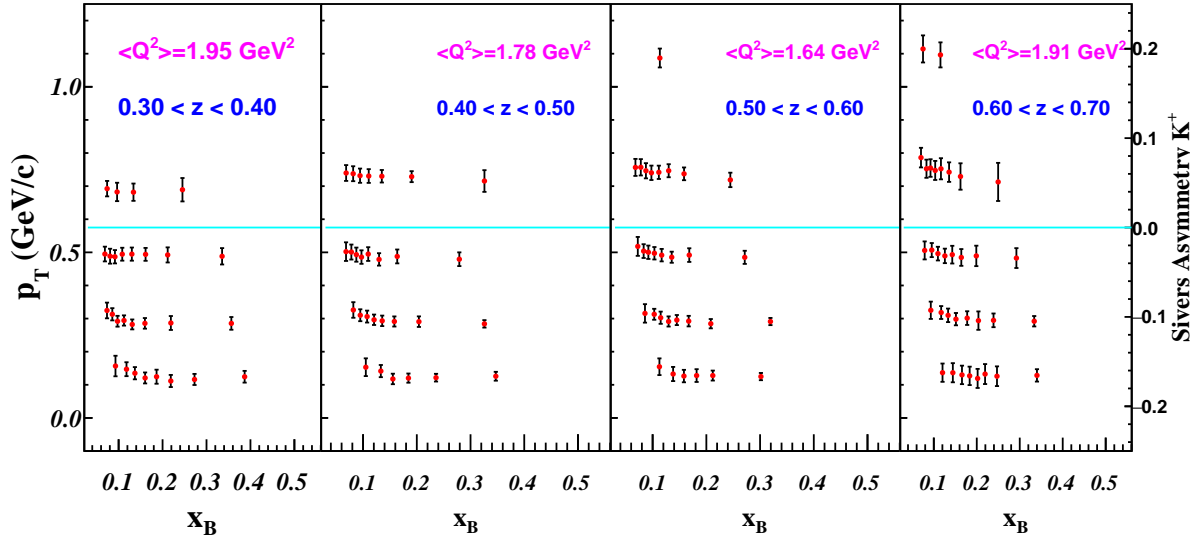


(a) $\bar{p}(e, e'K^+)X$

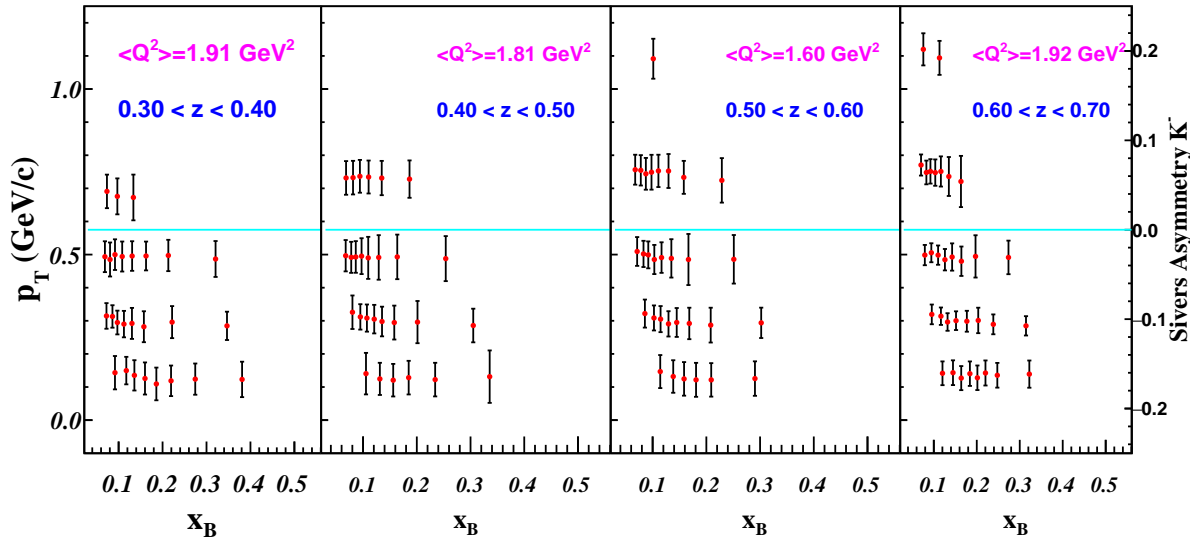


(b) $\bar{p}(e, e'K^-)X$

Figure 27: The 3D (z, p_T, x_B) binning projection and statistical uncertainties of the K^\pm Collins asymmetry ($A_{UT}^{\sin(\phi+\phi_S)}$) for the transversely polarized NH_3 (proton) target after combining the 11 GeV and 8.8 GeV simulation data. The sizes of the uncertainties are indicated by the Y axis on the right.



(a) $\bar{p}(e, e'K^+)X$



(b) $\bar{p}(e, e'K^-)X$

Figure 28: The 3D (z, p_T, x_B) binning projection and statistical uncertainties of the K^\pm Siverts asymmetry ($A_{UT}^{\sin(\phi-\phi_S)}$) for the transversely polarized NH_3 (proton) target after combining the 11 GeV and 8.8 GeV simulation data. The sizes of the uncertainties are indicated by the Y axis on the right.

4.4 Systematic Uncertainties

		${}^3\text{He}$ ("n")		NH_3 ("p")	
Sources	Type	Collins (K^\pm)	Sivers (K^\pm)	Collins (K^\pm)	Sivers (K^\pm)
Raw Asymmetry	absolute	1.4E-3	1.4E-3	6.5E-3	6.5E-3
Background Subtraction	relative	1.0%	1.0%	2.0%	2.0%
Detector Resolution	relative	<1.0%	<1.0%	<1.0%	<1.0%
Nuclear Effect	relative	4.0% ~ 5.0%	4.0% ~ 5.0%	—	—
Diffractive Vector Meson	relative	<1.0%	<1.0%	<1.0%	<1.0%
Radiative Correction	relative	2.0 ~ 3.0%	2.0 ~ 3.0%	2.0 ~ 3.0%	2.0 ~ 3.0%
Target Polarization	relative	3.0%+0.5%	3.0%+0.5%	3.0%+0.5%	3.0%+0.5%
Total	relative	6 ~ 7%	6 ~ 7%	4 ~ 5%	4 ~ 5%

Table 2: Systematic uncertainties on separating Collins and Sivers asymmetries from the kaon-SIDIS production with the polarized ${}^3\text{He}$ and NH_3 targets.

A dedicated detector system for the approved pion SoLID-SIDIS experiments [19,20,33] has been designed and will allow us to efficiently control the experimental related systematic uncertainties. In the last couple of years, the SoLID-SIDIS configuration has been continuously optimized to reach the experimental requirements. The full 2π azimuthal angular acceptance plays a huge role in reducing the systematic uncertainties during the extraction of different azimuthal asymmetries. The frequently rotating target spin orientation will also further suppress systematic uncertainties. The large signal-to-noise ratio, the high performance of the modern particle detectors, as well as strong expertise in data analysis from the 6 GeV Hall-A Transversity experiment and the CLAS experiment, will also help us to control the overall systematic uncertainty.

A good description of how to extract the physics results and control the systematic uncertainties was given in our pion SIDIS proposals which in principle can be directly applied to our kaon-SIDIS experiment. Nevertheless, we adopted the list of systematic uncertainties presented in the approved SoLID-SIDIS experiments, and their updated values base on our new study given in the SoLID-pCDR and later work. These uncertainties are given in Table 2.

We also consider the additional sources dedicated to the K^\pm measurements. Section 3.7 shows a 1% or better contamination with a 20 ps time resolution before considering the background effect. To be conservative, we assign a 3% systematic uncertainty due to the pion contamination.

5 Summary

We are proposing the measurement of K^\pm production in SIDIS with both the transversely polarized ${}^3\text{He}$ as effective neutron targets and transversely polarized NH_3 as proton targets. The experiment will run in parallel with the approved π^\pm -SIDIS experiments, E12-10-006 and E12-11-108, using the same SoLID-SIDIS configuration without modification. We will perform π^\pm/K^\pm separation using the PID cuts on the MRPC-TOF distributions and the Heavy-Gas Čerenkov Detector signals during the offline analysis. The high luminosity and large acceptance features of the SoLID allow us to simultaneously extract the K^\pm Collins asymmetry, Sivers asymmetry and maybe other TMD asymmetries.

Our only extra requirement is to extend the performance of the MRPC detectors to provide a time resolution of 20 ps for large-momentum kaons identification. We have proved that such a requirement

is reasonable and existing MRPC R&D projects have already achieved close or better timing resolution, although SoLID's high-rate environment will make the precise time measurement challenge. We also argued that even a slightly worse time resolution (30 ps) due to the high background rates still can help us to detect K^\pm up to 6 GeV/c and has very minimum impact to the physics projection.

Our new measurements will hence obtain precise kaon SIDIS data that can help us to cleanly isolate u and d quarks by combining with our pion SIDIS data. The new data will also have unique sensitivity to the TMDs of light sea-quarks. The study can directly provide important theoretical and experimental guidance to the SIDIS experiments on the future EIC which will perform precise measurements on the TMDs of sea quarks and gluons.

References

- [1] K. G. Wilson, *Phys. Rev. D* **10**, 2445 (1974).
- [2] C. D. Roberts and A. G. Williams, *Prog. Part. Nucl. Phys.* **33**, 477 (1994).
- [3] S. J. Brodsky, G. F. de Teramond, H. G. Dosch and J. Erlich, *Phys. Rep.* **584**, 1 (2015).
- [4] J. Ashman *et al.* [European Muon Collaboration], *Phys. Lett. B* **206**, 364 (1988).
- [5] J. Ashman *et al.* [European Muon Collaboration], *Nucl. Phys. B* **328**, 1 (1989).
- [6] J. J. Ethier, N. Sato and W. Melnitchouk, *Phys. Rev. Lett.* **119**, no. 13, 132001 (2017).
- [7] N. Sato *et al.* [Jefferson Lab Angular Momentum Collaboration], *Phys. Rev. D* **93**, no. 7, 074005 (2016).
- [8] D. de Florian, R. Sassot, M. Stratmann and W. Vogelsang, *Phys. Rev. Lett.* **113**, no. 1, 012001 (2014).
- [9] J. C. Collins, *Nucl. Phys. B* **396**, 161 (1993).
- [10] S. J. Brodsky, D. S. Hwang and I. Schmidt, *Phys. Lett. B* **530**, 99 (2002).
- [11] S. J. Brodsky, D. S. Hwang and I. Schmidt, *Nucl. Phys. B* **642**, 344 (2002).
- [12] J. C. Collins, *Phys. Lett. B* **536**, 43 (2002).
- [13] D. W. Sivers, *Phys. Rev. D* **43**, 261 (1991).
- [14] T. Liu, Z. Zhao and H. Gao, *Phys. Rev. D* **97**, no. 7, 074018 (2018).
- [15] A. Bacchetta, F. Conti and M. Radici, *Phys. Rev. D* **78**, 074010 (2008).
- [16] J. She, J. Zhu and B. Q. Ma, *Phys. Rev. D* **79**, 054008 (2009).
- [17] C. Lorce and B. Pasquini, *Phys. Lett. B* **710**, 486 (2012).
- [18] T. Liu and B. Q. Ma, *Phys. Lett. B* **741**, 256 (2015).
- [19] Approved SoLID SIDIS experiment E12-10-006, "Target Single Spin Asymmetry in Semi-Inclusive Deep-Inelastic ($e, e'\pi^\pm$) Reaction on a Transversely Polarized ^3He Target at 11 GeV", https://www.jlab.org/exp_prog/proposals/14/E12-10-006A.pdf.

- [20] Approved SoLID SIDIS experiment E12-11-108, “Target Single Spin Asymmetry in Semi-Inclusive Deep-Inelastic ($e, e'\pi^\pm$) Reactions on a Transversely Polarized Proton Target”, https://www.jlab.org/exp_prog/proposals/11/PR12-11-108.pdf.
- [21] Approved SBS SIDIS experiment E12-09-018, “Measurement of Semi-Inclusive Pion and Kaon electroproduction in the DIS Regime on a Transversely Polarized ^3He Target using the Super BigBite and BigBite Spectrometers in Hall A”, <http://hallaweb.jlab.org/collab/PAC/PAC38/E12-09-018-SIDIS.pdf>.
- [22] Conditionally approved CLAS12 SIDIS experiment C12-11-111, “Transverse spin effects in SIDIS at 11 GeV with a transversely polarized target using the CLAS12 Detector”, https://www.jlab.org/exp_prog/proposals/12/C12-11-111.pdf.
- [23] A. Airapetian *et al.* [HERMES Collaboration], *Phys. Lett. B* **693**, 11 (2010).
- [24] C. Adolph *et al.* [COMPASS Collaboration], *Phys. Lett. B* **744**, 250 (2015).
- [25] X. Qian *et al.* [Jefferson Lab Hall A Collaboration], *Phys. Rev. Lett.* **107**, 072003 (2011).
- [26] Y. X. Zhao *et al.* [Jefferson Lab Hall A Collaboration], *Phys. Rev. C* **90**, no. 5, 055201 (2014).
- [27] A. Bacchetta, U. D’Alesio, M. Diehl and C. A. Miller, *Phys. Rev. D* **70**, 117504 (2004).
- [28] A. Bacchetta, M. Diehl, K. Goeke, A. Metz, P. J. Mulders and M. Schlegel, *J. High Energy Phys.* **02** (2007) 093.
- [29] M. Diehl and S. Sapeta, *Eur. Phys. J. C* **41**, 515 (2005).
- [30] M. Boglione, J. Collins, L. Gamberg, J. O. Gonzalez-Hernandez, T. C. Rogers and N. Sato, *Phys. Lett. B* **766**, 245 (2017).
- [31] T. C. Rogers, Mapping the partonic kinematics of semi-inclusive deep inelastic scattering, in prepare; and private communications.
- [32] SoLID Collaboration, “Solenoidal Large Intensity Device Preliminary Conceptual Design Report”, http://hallaweb.jlab.org/12GeV/SoLID/download/doc/solid_precdr_2017.pdf.
- [33] Approved SoLID SIDIS experiment E12-11-007, “Asymmetries in Semi-Inclusive Deep-Inelastic ($e, e'\pi^\pm$) Reactions on a Longitudinally Polarized ^3He Target at 8.8 and 11 GeV”, https://www.jlab.org/exp_prog/PACpage/PAC37/proposals/Proposals/New%20Proposals/PR-11-007.pdf.
- [34] Approved SoLID J/ψ experiment E12-12-006A, “Near Threshold Electroproduction of J/ψ at 11 GeV”, https://www.jlab.org/exp_prog/proposals/12/PR12-12-006.pdf.
- [35] Approved SoLID SIDIS experiment E12-10-006A, “Dihadron Electroproduction in DIS with Transversely Polarized ^3He Target at 11 and 8.8 GeV”, https://www.jlab.org/exp_prog/proposals/14/E12-10-006A.pdf.
- [36] Approved SoLID SIDIS experiment E12-11-108A, “Target Single Spin Asymmetry Measurements in the Inclusive Deep-Inelastic $\vec{N}(e, e')$ Reaction on Transversely Polarized Proton and Neutron (^3He) Targets using the SoLID Spectrometer”, https://www.jlab.org/exp_prog/proposals/14/E12-11-108A_E12-10-006A.pdf.

- [37] Approved SoLID PVDIS experiment E12-10-007, “Precision Measurement of Parity-violation in Deep Inelastic Scattering Over a Broad Kinematic Range”, https://www.jlab.org/exp_prog/PACpage/PAC37/proposals/Proposals/Previously%20Approved/E12-10-007.pdf.
- [38] Approved SoLID GPD experiment E12-10-006B, “Measurement of Deep Exclusive π^\pm Production using a Transversely Polarized ^3He Target and the SoLID Spectrometer”, https://www.jlab.org/exp_prog/proposals/17/E12-10-006B.pdf.
- [39] Y. Wang *et al.*, “A MRPC prototype for SOLID-TOF in JLab,” *JINST* **8**, P03003 (2013).
- [40] ALICE Collaboration, “The ALICE experiment at the CERN LHC”, *JINST* **3** (2008) S08002
- [41] S. An, *et al.*, *Nucl. Instrum. Meth.* **A594** (2008) 39-43
- [42] L. Doroud, *et al.*, *Nucl. Instrum. Meth.* **A629** (2011) 106-110
- [43] Crispin Williams, *et. al.*, https://indico.cern.ch/event/13750/contributions/146271/attachments/113687/161504/williams-alice_tof.pdf
- [44] EIC RD2013-5, “R&D Proposal for (Sub) 10 Picosecond Timing Detectors at the EIC”. https://wiki.bnl.gov/conferences/images/3/38/PSTOF_EIC_July2014.pdf
- [45] Fuyue Wang, Dong Han, Yi Wang, Yancheng Yu, Baohong Guo, and Yuanjing Li, ”A neural network based algorithm for MRPC time reconstruction.”, arXiv:1805.02833
- [46] W. Riegler, *et al.*, *Nucl. Instrum. Meth.* **A500** (2003) 144-162
- [47] S. Ramo, *Proc.Ire.* **27** (1939) 584-585
- [48] Z. Ye, N. Sato, K. Allada, T. Liu, J-P Chen, H. Gao, Z. Kang, A. Prokudin, P. Sun, and F. Yuan, *Phys. Lett. B* **767**, 91 (2017).
- [49] GetSIDIS, a SIDIS Monte Carlo Generator, <https://github.com/yezhihong/GetSIDIS>.
- [50] A. Accardi, L. T. Brady, W. Melnitchouk, J. F. Owens and N. Sato, *Phys. Rev. D* **93**, no. 11, 114017 (2016), <https://www.jlab.org/theory/cj/index.html>.
- [51] D. de Florian, R. Sassot and M. Stratmann, *Phys. Rev. D* **75**, 114010 (2007).